

Autonomous Navigation and Station-Keeping on Near-Rectilinear Halo Orbits

Yuri Shimane*

University of California, Irvine, Irvine, CA 92617

Karl Berntorp[†], Stefano Di Cairano[‡], and Avishai Weiss[§]

Mitsubishi Electric Research Laboratories (MERL), Cambridge, Massachusetts, 02139

This article develops an optical navigation (OPNAV) and station-keeping pipeline for the near-rectilinear halo orbit (NRHO) in high-fidelity ephemeris model dynamics. The pipeline involves synthetic images used by the non-iterative horizon-based OPNAV algorithm, fed into an extended Kalman filter. The state estimate is used by a controller to maintain the spacecraft's motion within the vicinity of a reference NRHO. We study differential correction-based and minimization-based implementations of the x -axis crossing control scheme, and propose an improved targeting prediction scheme by incorporating the filter's state covariance with an unscented transform. We also introduce a hysteresis mechanism, which improves station-keeping cost and provides insight into the difference in performance between the differential correction-based and minimization-based approaches. We perform Monte-Carlo experiments to assess the pipeline's tracking and ΔV performances. We report several key findings, including the variability of the filter performance with the sensor field of view and measurement locations, station-keeping cost reduction achieved by the unscented transform-based prediction and hysteresis, as well as variability of the cumulative ΔV as a function of maneuver location due to the periodic structure in the OPNAV-based filter's estimation accuracy.

Nomenclature

A/m	=	solar radiation pressure area-to-mass ratio, m^2/kg
C_r	=	solar radiation pressure coefficient
\mathcal{F}_{EM}	=	Earth-Moon rotating frame centered at the Moon
\mathcal{F}_{I}	=	inertial frame centered at the Moon
\mathcal{F}_{P}	=	Moon's principal axes frame

*Assistant Professor, Department of Mechanical and Aerospace Engineering, AIAA Member; Y. Shimane was with MERL at the time of this research.

[†]Chewy Robotics; K. Berntorp was with MERL at the time of this research.

[‡]Distinguished Research Scientist, AIAA Member.

[§]Senior Principal Research Scientist, AIAA Member.

f	= spacecraft dynamics
f	= camera focal length, mm
FOV	= field of view, deg
K	= filter Kalman gain
m	= number of points lying on the lit limb
NRHO	= near-rectilinear halo orbit
Q	= filter process noise
R_y	= measurement covariance
r	= spacecraft inertial position vector, km
T_B^A	= transformation matrix from frame A to frame B
t	= time, s
v	= spacecraft inertial velocity vector, km/s
$v_{x,tol}$	= v_x targeting tolerance, m/s
$v_{x,trig}$	= v_x trigger threshold, m/s
y	= measurement
κ	= camera calibration matrix
Σ	= filter state covariance
θ	= spacecraft inertial state vector
θ	= true anomaly, deg
Φ	= state transition matrix
Ψ	= targeted subset of state

I. Introduction

A key challenge of operating space assets in cislunar space is the vast distance from the Earth. The distance makes frequent communication and navigational updates to cislunar spacecraft a challenge due to the scarcity and congestion of ground-based infrastructures, necessitating autonomous capability for guidance, navigation, and control (GNC). A particular orbit of interest is the 9:2 resonant near-rectilinear halo orbit (NRHO) about the Earth-Moon L2 point [1–3], due to its planned use for the upcoming lunar space station, or *Gateway*, humanity’s next outpost in space.

Regular station-keeping (SK) maneuvers, also referred to as orbit maintenance maneuvers, are required for spacecraft flying along the NRHO due to the orbit’s unstable modes. SK is required at an appropriate cadence in order to cancel the unstable modes in the presence of errors in state estimation, dynamics model, and control. As traffic on the NRHO is expected to increase, autonomous GNC along this orbit is of critical importance, both to reduce reliance on ground-based

navigation updates in nominal operations contexts, as well as to ensure a reliable onboard GNC capability in case of off-nominal scenarios such as communication failures. Today, with the lack of a dedicated cislunar position, navigation, and timing (PNT) architecture, horizon-based optical navigation (OPNAV) [4–6] is a suitable measurement source that may be acquired and processed onboard a spacecraft along the NRHO. A number of prior simulation-based works considered autonomous navigation using horizon-based OPNAV on lunar libration point orbits (LPOs) [7, 8], as well as specifically on the NRHO [9, 10], but without consideration of SK activities. Several recent missions have successfully demonstrated horizon-based OPNAV for orbit determination in cislunar flight: the Orion spacecraft during the Artemis I mission [11], the LONESTar experiment during the Lunar Flashlight mission [12], and the CAPSTONE mission [13].

There has been significant focus on SK algorithms and their performance under orbit determination error; Shirobokov et al. [14] provides a survey of the various SK schemes and for LPOs in various dynamical regimes. Oguri [15] demonstrates navigation with numerically simulated horizon-based OPNAV and SK based on an optimization-based pre-computed feedback policy. In the context of SK for NRHOs, the x -axis crossing control is known to perform favorably [16–19]; in the recent CAPSTONE mission, this strategy was successfully deployed on the NRHO [20], and has been chosen as the approach for the Gateway [19].

In this work, we evaluate the feasibility and performance of autonomous GNC along NRHO by developing an end-to-end pipeline that consists of a navigation filter relying solely on measurements from processing realistic synthetic images of the Moon, and a SK algorithm that use the recursively filtered state estimate to compute control actions. The synthetic images are generated using a rendering setup previously developed by the authors [21], and are processed to generate position measurements using the state-of-the-art non-iterative horizon-based OPNAV algorithm [4, 5]. We augment the fidelity of the measurement covariance expression of the horizon-based OPNAV algorithm by accounting for the attitude error of the camera. We compare two variants of the x -axis crossing control, namely the traditional differential correction-based approach [16, 17, 19] and the optimization-based approach [22]. In addition, we propose an unscented transform (UT)-based targeting scheme that uses the filter’s state covariance information to improve the state prediction. We also introduce hysteresis by setting a higher state violation threshold for executing control than the state violation threshold that the x -axis crossing control aims to satisfy. Both the UT-based targeting and hysteresis can be readily implemented within the x -axis crossing control scheme, and are found to result in tangible cumulative SK ΔV cost reduction.

The GNC pipeline is used to conduct multiple Monte-Carlo experiments in which measurement collection and controller hyperparameters are varied. We report the levels of navigation accuracy that can be achieved by horizon-based OPNAV, and quantify its limitations. We compare differential correction-based and minimization-based implementations of the x -axis crossing control and show the significant performance difference that arises due to the myopic per-maneuver SK optimization as an approximation of the infinite-horizon cumulative SK cost. Finally, using the pipeline, we study the sensitivity of the cumulative SK cost to SK maneuver location along the NRHO.

The remainder of this paper is organized as follows. Section II introduces the full-ephemeris dynamics and the key dynamical properties of the NRHO. In Section III, the horizon-based OPNAV and the navigation filter implemented in this work are introduced. Section IV concerns the x -axis crossing controller, along with the modifications and augmentations that we propose. Section V provides results based on the navigation filter incorporating OPNAV measurements without any SK. Next, in Section VI, the SK schemes are compared with different levels of assumed state estimation errors. Section VII provides end-to-end simulation results with both the OPNAV-based navigation filter and the SK algorithms. Finally, conclusions to this work are given in Section VIII.

II. Preliminaries

We first introduce the high-fidelity ephemeris model in which the spacecraft's motion is studied. Then, we briefly discuss the NRHO, pointing out characteristics that pertain to OPNAV-based navigation and SK.

A. Equations of Motion

We consider the motion of the spacecraft in cislunar space under the effect of gravitational forces of the Moon, Earth and Sun, along with J2 perturbation from the Moon and solar radiation pressure (SRP), in a Moon-centered inertial frame \mathcal{F}_1 . The equations of motion are given by

$$\dot{\boldsymbol{\theta}} = \begin{bmatrix} \dot{\mathbf{r}} \\ \dot{\mathbf{v}} \end{bmatrix} = \mathbf{f}(t, \boldsymbol{\theta}) = \begin{bmatrix} \mathbf{v} \\ -\frac{\mu}{r^3} \mathbf{r} + \mathbf{a}_{J2}(t, \mathbf{r}) + \sum_i \mathbf{a}_{N_i}(t, \mathbf{r}) + \mathbf{a}_{\text{SRP}}(t, \mathbf{r}) \end{bmatrix}, \quad (1)$$

where $\mathbf{r} \in \mathbb{R}^3$ is the position vector of the spacecraft with respect to an unforced particle at the origin of \mathcal{F}_1 , $\mathbf{v} \triangleq \dot{\mathbf{r}} \in \mathbb{R}^3$ is the rate of change of \mathbf{r} in \mathcal{F}_1 , and $\boldsymbol{\theta}^T = [\mathbf{r}^T, \mathbf{v}^T] \in \mathbb{R}^6$ is the state vector. In the acceleration terms on the right-hand side, $r = \|\mathbf{r}\|$ is the distance from the center of the Moon to the spacecraft, μ is the standard gravitational parameter of the Moon, \mathbf{a}_{J2} is the perturbing acceleration due to the J2 coefficient of the lunar spherical harmonic gravitational model, \mathbf{a}_{N_i} is the third-body perturbing acceleration of body i , and \mathbf{a}_{SRP} is the perturbing acceleration due to SRP. In

this work, we consider third-body perturbations due to the Earth and the Sun. The perturbation terms are given by

$$\begin{aligned}
\mathbf{a}_{J_2}(t, \mathbf{r}) &= \mathbf{T}_I^P \left(-\frac{3\mu J_2 R^2}{2r^5} \begin{bmatrix} \left(1 - 5\frac{z_P^2}{r^2}\right) x_P \\ \left(1 - 5\frac{z_P^2}{r^2}\right) y_P \\ \left(3 - 5\frac{z_P^2}{r^2}\right) z_P \end{bmatrix} \right), \\
\mathbf{a}_{N_i}(t, \mathbf{r}) &= -\mu_i \left(\frac{\mathbf{r} - \mathbf{d}_i}{\|\mathbf{r} - \mathbf{d}_i\|^3} + \frac{\mathbf{d}_i}{d_i^3} \right), \\
\mathbf{a}_{\text{SRP}}(t, \mathbf{r}) &= P_{\text{Sun}} \left(\frac{\|\mathbf{d}_{\text{Earth}} - \mathbf{d}_{\text{Sun}}\|_2}{r_{\text{Sun}}} \right)^2 C_r \frac{A}{m} \frac{\mathbf{r}_{\text{Sun}}}{r_{\text{Sun}}},
\end{aligned} \tag{2a}$$

where $\mathbf{T}_I^P \in \mathbb{R}^{3 \times 3}$ is the transformation matrix from the Moon's principal axes frame \mathcal{F}_P to \mathcal{F}_I , J_2 is the oblateness coefficient of the Moon, R is the equatorial radius of the Moon, and subscript $(\cdot)_P$ denote position components in \mathcal{F}_P ; μ_i is the gravitational parameter of body i , and \mathbf{d}_i is the position of body i ; P_{Sun} is the SRP magnitude at 1 AU, C_r is the radiation pressure coefficient, and A/m is the area-to-mass ratio.

The linearized solution to equation (1) in the vicinity of a reference state $\bar{\boldsymbol{\theta}}$ at time t is given by

$$\delta\boldsymbol{\theta}(t) = \frac{\partial\boldsymbol{\theta}(t)}{\partial\bar{\boldsymbol{\theta}}(t_0)} \delta\boldsymbol{\theta}(t_0), \tag{3}$$

where $\delta\boldsymbol{\theta}(t_0)$ denotes the initial deviation from the initial reference state $\bar{\boldsymbol{\theta}}(t_0)$ at time t_0 . The partial $\partial\boldsymbol{\theta}(t)/\partial\bar{\boldsymbol{\theta}}(t_0)$ is the state-transition matrix (STM) denoted by the shorthand $\boldsymbol{\Phi}(t, t_0)$, obtained through the nonlinear integration of the initial value problem

$$\begin{cases} \dot{\boldsymbol{\Phi}}(t, t_0) = \frac{\partial \mathbf{f}(t, \boldsymbol{\theta})}{\partial \bar{\boldsymbol{\theta}}} \boldsymbol{\Phi}(t, t_0), \\ \boldsymbol{\Phi}(t_0, t_0) = \mathbf{I}_6. \end{cases} \tag{4}$$

B. Near-Rectilinear Halo Orbit

Libration point orbits (LPO), periodic motions revolving around libration points, offer the option for spacecraft to be placed in unique periodic regimes in cislunar space that are otherwise unattainable by classical Keplerian orbits about the Earth or the Moon. There exist multiple families of LPOs, each with varying characteristics in terms of their spatial location, energy, and/or stability, and the NRHOs are a subset of the so-called halo orbit families about the L1/L2 points with bounded linear stability. For details on the dynamic structure of NRHOs, see [2, 3] and references therein. In this work, we focus on the 9:2 resonant NRHO of the Gateway, which completes 9 revolutions over 2 synodic periods of the Moon.

While periodic motions may be numerically constructed in simplified models such as the circular restricted three-body problem, the analogous motion in the full-ephemeris model is only quasi-periodic and contains unstable modes, thus requiring SK corrections to maintain the spacecraft on the desired orbit. Integrating motion along the NRHO is further complicated by the relatively low perilunes of around 3000 km, as numerical integration errors get amplified during the transits through perilunes, where the dominant acceleration, proportional to $1/r^2$, has high sensitivities. The compounding effects of the inherent dynamical, as well as numerical, instabilities, necessitate a numerical integrator that is efficient with tight error tolerances. In this work, we make use of the explicit embedded Runge-Kutta Prince-Dormand 9(8) from Verner [23] in the GNU scientific library (GSL) [24].

C. System Architecture for Optical Navigation and Station-Keeping

To validate autonomous navigation and SK on an NRHO, we develop a simulation environment that generates synthetic images of the Moon, processes the images to generate position measurements and measurement covariances, estimates the spacecraft state using a navigation filter, and computes orbital correction maneuvers using an SK controller. This framework is illustrated in Figure 1.

Starting with the measurement block, synthetic images are generated using Blender; details of this implementation are provided in [21]. The image is then processed using the Christian-Robinson algorithm, which is a horizon-based, non-iterative method for generating a position measurement \mathbf{r}_p , along with an analytical expression for the measurement covariance \mathbf{P}_{r_p} . The measurement and measurement covariance are fed to the navigation filter; for simulation purposes, we keep track of both the filter's state estimate $\hat{\boldsymbol{\theta}}$ as well as the true state $\boldsymbol{\theta}$. The synthetic imaging block uses $\boldsymbol{\theta}$ to place the camera, while $\hat{\boldsymbol{\theta}}$ is used to point the camera toward the perceived location of the Moon. The control block on the bottom right is only given $\hat{\boldsymbol{\theta}}$ and \mathbf{P}_{r_p} to compute a control command \mathbf{u} . The state estimation assumes that \mathbf{u} is executed, while in fact a corrupted $\mathbf{u} + \delta\mathbf{u}$ is executed on the true state $\boldsymbol{\theta}$.

III. Autonomous Navigation with Optical Measurements

We first provide an overview of the horizon-based OPNAV scheme. We adopt the non-iterative Christian-Robinson algorithm [4] due to its superior performance over other iterative, ellipse-fitting-based variants [25]. We develop a measurement covariance expression based on [4] which accounts for attitude uncertainty in addition to the error associated with detecting the lit limb within the image. Then, we briefly discuss the simulation environment developed in Blender in our previous work [21]. Finally, we describe the dynamic filter employed with the OPNAV measurements for simulating autonomous navigation.

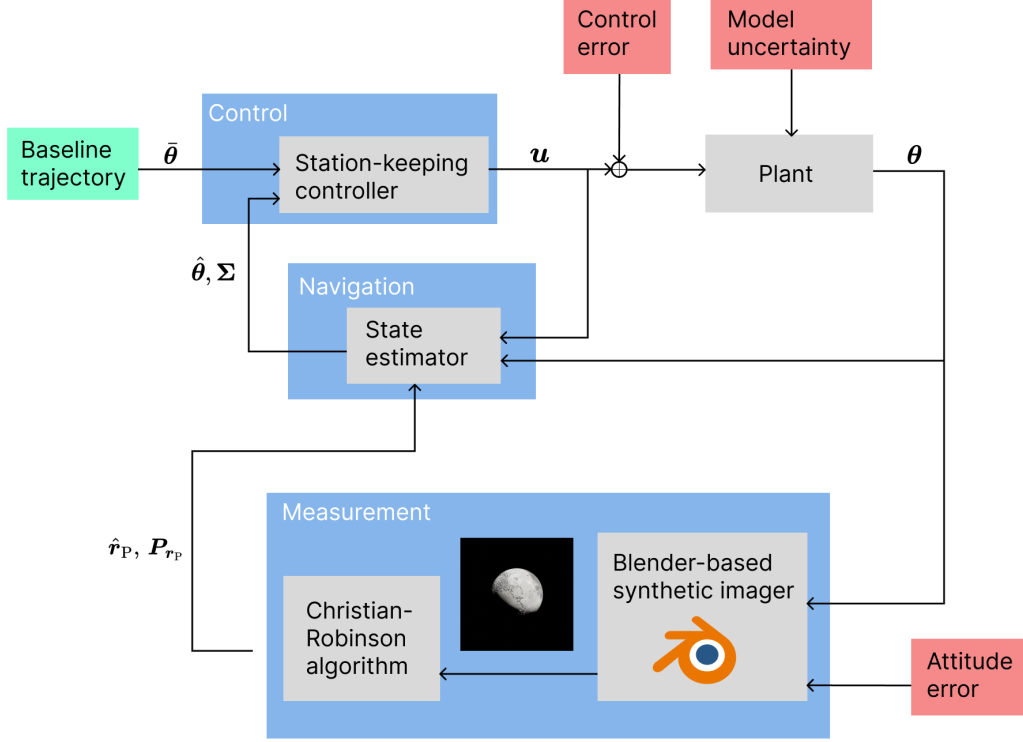


Fig. 1 Overview of optical navigation-based station-keeping architecture and simulation environment

A. Horizon-Based Optical Navigation

We consider the horizon-based OPNAV algorithm for computing the position vector of the spacecraft with respect to the imaged body assuming the camera attitude, defined by the camera frame \mathcal{F}_C , is known. This assumption is built on the fact that spacecraft attitude can be computed with high precision using star trackers. The small error on the spacecraft's attitude is incorporated into the image generation process, and the measurement covariance expression is updated from the expression provided in [4] to reflect this source of error. The algorithm also requires ephemerides of the Moon and the Sun, as well as the radii of the Moon; these are assumed to be stored on the onboard computer.

1. Christian-Robinson Algorithm

The Christian-Robinson algorithm [4] provides both the position vector estimate as well as an analytical expression for the position measurement covariance. While a short overview is provided here for completeness, a full description is available for the Cholesky decomposition variant in [4] and for the Singular Value Decomposition (SVD) variant in [5]. Starting with the m pixel coordinates along the lit limb $\{u_i, v_i\}_{i=1}^m$ of the Moon, each point is projected onto a point on

the image plane s_i by using the intrinsic camera calibration matrix κ [5, 6, 26]

$$s_i = \kappa^{-1} \begin{bmatrix} u_i \\ v_i \\ 1 \end{bmatrix}. \quad (5)$$

Then, using the SVD, the horizon-based OPNAV problem is transformed from being relative to a triaxial ellipsoid to being relative to a unit sphere via

$$\bar{s}_i = \mathbf{Q} \mathbf{T}_P^C s_i, \quad (6)$$

where $\mathbf{Q} = \text{diag}(1/a, 1/b, 1/c)$ with a, b, c the body's principal axes, and $\mathbf{T}_P^C \in \mathbb{R}^{3 \times 3}$ is the transformation matrix from \mathcal{F}_C to \mathcal{F}_P . Finally, defining $\bar{s}'_i = \bar{s}_i / \|\bar{s}_i\|$, the position of the spacecraft in the camera frame is obtained by solving the linear least-squares problem

$$\begin{bmatrix} \bar{s}'_1{}^T \\ \bar{s}'_2{}^T \\ \vdots \\ \bar{s}'_m{}^T \end{bmatrix} \mathbf{n} = \mathbf{H} \mathbf{n} = \mathbf{1}_{m \times 1}. \quad (7)$$

The matrix \mathbf{H} is the vertical concatenation of $\bar{s}'_i{}^T$ for $i = 1, \dots, m$. The position vector of the spacecraft in \mathcal{F}_C is given by

$$\hat{\mathbf{r}}_C = -(\mathbf{n}^T \mathbf{n} - 1)^{-(1/2)} \mathbf{T}_C^P \mathbf{Q}^{-1} \mathbf{n}, \quad (8)$$

which is transformed to \mathcal{F}_P via

$$\hat{\mathbf{r}}_P = \mathbf{T}_P^C \hat{\mathbf{r}}_C = -(\mathbf{n}^T \mathbf{n} - 1)^{-(1/2)} \mathbf{Q}^{-1} \mathbf{n}, \quad (9)$$

where $\mathbf{T}_P^C \in \mathbb{R}^{3 \times 3}$ is the transformation matrix from \mathcal{F}_P to \mathcal{F}_C .

2. Analytical Measurement Covariance Under Attitude Uncertainty

Following Christian and Robinson [4], we compute the covariance of the position measurement, in the presence of error associated with detecting the lit limb within the image, quantified in terms of the “standard deviation of an observed horizon point in units of pixels” σ_{pix} . This model assumes a perfect attitude knowledge, and as a consequence a perfect knowledge of the transformation matrix \mathbf{T}_C^P . However, in reality, the camera will have some unknown misalignment due to the imperfection of the estimated attitude, the mounting process of the hardware, and the vibration during launch. To this end, we develop an expression for the measurement covariance of the position in \mathcal{F}_P , denoted by \mathbf{P}_{r_P} , that

incorporates both the error introduced by the limb detection process, as well as the imperfect attitude knowledge.

Taking the variation of (9) with respect to both \mathbf{n} and ϕ ,

$$\delta \mathbf{r}_P = \mathbf{F} \delta \mathbf{n} + \mathbf{G} \delta \phi, \quad (10)$$

where \mathbf{F} and \mathbf{G} are given by

$$\mathbf{F} = - \left(\mathbf{n}^T \mathbf{n} - 1 \right)^{-(1/2)} \mathbf{Q}^{-1} \left(\mathbf{I}_{3 \times 3} - \frac{\mathbf{n} \mathbf{n}^T}{\mathbf{n}^T \mathbf{n} - 1} \right), \quad (11)$$

$$\mathbf{G} = \mathbf{T}_P^C [\mathbf{r}_C \times], \quad (12)$$

$[\cdot \times]$ is the skew-symmetric matrix $[\mathbf{a} \times] \mathbf{b} = \mathbf{a} \times \mathbf{b}$, and d_x is the pixel pitch in terms of pixels per radian. The covariance of $\hat{\mathbf{r}}_P$ is given by

$$\mathbf{P}_{r_P} = \mathbb{E}[\delta \hat{\mathbf{r}}_P \delta \hat{\mathbf{r}}_P^T] = \mathbf{F} \mathbf{P}_n \mathbf{F}^T + \mathbf{G} \mathbf{P}_\phi \mathbf{G}^T, \quad (13)$$

where \mathbf{P}_n is the covariance of the vector \mathbf{n} , and \mathbf{P}_ϕ is the covariance of the camera attitude. The expression for \mathbf{P}_ϕ is given by

$$\mathbf{P}_\phi = \sigma_\phi^2 \mathbf{I}_{3 \times 3}. \quad (14)$$

An approximation for \mathbf{P}_n developed in [27] for Cholesky decomposition is adapted to the SVD via

$$\mathbf{P}_n = \left(\mathbf{H}^T \mathbf{R}_y \mathbf{H} \right)^{-1}, \quad (15)$$

where $\mathbf{R}_y \in \mathbb{R}^{m \times m}$ is the covariance of the residuals of the least-squares problem (7), given by

$$\begin{aligned} \mathbf{R}_y &= \text{diag}(\sigma_{y_1}^2, \dots, \sigma_{y_m}^2), \\ \sigma_{y_i} &= \mathbf{J}_i \mathbf{Q} \mathbf{T}_P^C \mathbf{R}_s \mathbf{T}_C^P \mathbf{Q}^T \mathbf{J}_i^T, \end{aligned} \quad (16)$$

\mathbf{R}_s is the covariance of the horizon measurements, approximated by

$$\mathbf{R}_s \approx \left(\frac{\sigma_{\text{pix}}}{d_x} \right)^2 \begin{bmatrix} 1 & 0 & 0 \\ 0 & 1 & 0 \\ 0 & 0 & 0 \end{bmatrix}, \quad (17)$$

σ_{pix} is the standard deviation of an observed horizon point in units of pixels [27], and \mathbf{J}_i is given by

$$\mathbf{J}_i = \frac{1}{\|\bar{\mathbf{s}}_i\|} \mathbf{n}^T (\mathbf{I}_{3 \times 3} - \bar{\mathbf{s}}_i' \bar{\mathbf{s}}_i'^T). \quad (18)$$

The measurement covariance expression (13) is validated using a Monte-Carlo experiment. At a fixed range of 70 000 km from the Moon, each Monte-Carlo sample is computed as follows:

- 1) Generate random transformation matrix \mathbf{T}_P^C .
- 2) Generate 100 limb pixel coordinates $\{u_i, v_i\}_{i=1}^{100}$ along the true limb of the body, located at equal angle intervals over a circular sector of 140° , perturbed by individually drawing a realization of σ_{pix}

$$\{u_i, v_i\} = \{u_i, v_i\}_{\text{true}} + \{\delta u_i, \delta v_i\} \quad i = 1, \dots, m, \quad (19)$$

where $\delta u_i, \delta v_i \sim \mathcal{N}(0, \sigma_{\text{pix}})$.

- 3) Construct the attitude perturbation matrix $\delta \mathbf{T} \in \mathbb{R}^{3 \times 3}$ using the Rodrigues' rotation formula

$$\delta \mathbf{T} = \cos(\delta \phi) \mathbf{I}_3 + \sin(\delta \phi) \mathbf{i}^\times + [1 - \cos(\delta \phi)] \mathbf{i} \mathbf{i}^T, \quad \mathbf{i} = \frac{1}{\sqrt{i_x^2 + i_y^2 + i_z^2}} \begin{bmatrix} i_x \\ i_y \\ i_z \end{bmatrix}, \quad (20)$$

where $\delta \phi \sim \mathcal{N}(0, \sigma_\phi^2)$, $i_x, i_y, i_z \sim \mathcal{U}(-1, 1)$, and \mathbf{i}^\times is the skew-symmetric form of \mathbf{i} .

- 4) Compute true position in the planet frame

$$\mathbf{r}_P = \delta \mathbf{T} \mathbf{T}_P^C \begin{bmatrix} 0 \\ 0 \\ -70000 \end{bmatrix}. \quad (21)$$

- 5) Compute position estimate $\hat{\mathbf{r}}_P$ and covariance \mathbf{P}_{r_P} from Christian-Robinson algorithm using \mathbf{T}_P^C .
- 6) Compute error as $\hat{\mathbf{r}}_P - \mathbf{r}_P$.

Using $\sigma_{\text{pix}} = 0.5$ pixel and $\sigma_\phi = 15$ arcsec, the distribution of the actual measurement error is shown in Figure 2. Based on the 10 000 samples, we find 66.060% fall within $1\text{-}\sigma$, 94.710% fall within $2\text{-}\sigma$, and 99.730% fall within $3\text{-}\sigma$ as predicted by \mathbf{P}_{r_P} .

B. Simulation Environment for Horizon-Based Optical Navigation

The simulation environment is developed using Blender [28], an open-source rendering engine. The development process of the simulation environment is detailed in our prior paper [21]. Points on the image corresponding to the lit limb of the Moon are found through a three-step process following [5], consisting of (i) creating a mask centered around approximate lit limb locations found by scanning the image along the projected direction of the illumination

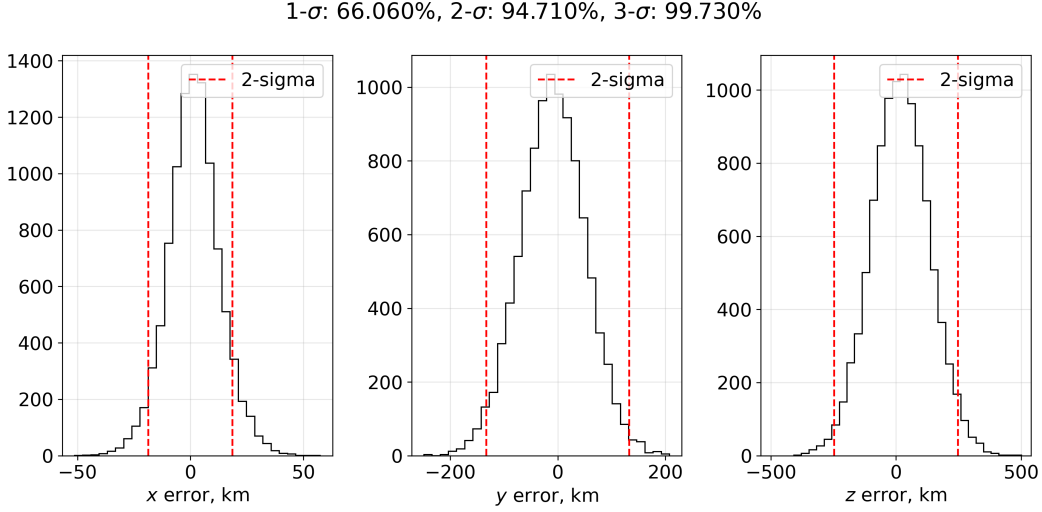


Fig. 2 Monte-Carlo results for measurement distributions of horizon-based OPNAV position under attitude error, using 10000 tries with $\sigma_{\text{pix}} = 0.5$ pixel, $\sigma_{\phi} = 15$ arcsec. Red lines indicate empirical 2- σ of the samples.

vector of the Sun, followed by (ii) applying a mask on edge points detected using the Canny edge detection algorithm, and finally (iii) applying a Zernike moment-based refinement scheme to correct the pixel-level point from (ii) down to subpixel-level locations using local mini patches around each point.

C. Navigation Filter

The operation of a spacecraft requires a navigation filter to keep track of the best state estimate given measurements that may only include a subset of the state components. Due to the non-negligible nonlinearity of the dynamics, the traditional Kalman filter is insufficient for accurately predicting the state. Thus, the extended Kalman filter (EKF) or the unscented Kalman filter (UKF) is more effective, providing a suitable trade-off between capturing the nonlinearity of the dynamics and the computational burdens.

In the context of spaceflight, the EKF has been successfully applied in multiple missions [29]. Through preliminary studies, we found that EKF and UKF result in nearly identical navigation performance assuming a measurement update cadence of a few images per revolution. Thus, we adopt the EKF for navigation. Nevertheless, we also introduce the UT-based prediction, as its prediction scheme is leveraged for the design of the SK controller.

1. Prediction in Extended Kalman Filter

To account for the uncertainties in (1), we include an additive process noise [30]. The prediction step of the EKF is given by

$$\hat{\boldsymbol{\theta}}_{j|j-1} = \hat{\boldsymbol{\theta}}_{j-1|j-1} + \int_{t_{j-1}}^{t_j} \mathbf{f}(\tau, \hat{\boldsymbol{\theta}}_{j-1}(\tau)) d\tau, \quad (22a)$$

$$\boldsymbol{\Sigma}_{j|j-1} = \boldsymbol{\Phi}(t_j, t_{j-1}) \boldsymbol{\Sigma}_{j-1|j-1} \boldsymbol{\Phi}^T(t_j, t_{j-1}) + \mathbf{Q}_j. \quad (22b)$$

The process noise is modeled as an unbiased random process with covariance

$$\mathbf{Q}_j = \sigma_u^2 \begin{bmatrix} \frac{1}{3} h_j^3 \mathbf{I}_{3 \times 3} & \frac{1}{2} h_j^2 \mathbf{I}_{3 \times 3} \\ \frac{1}{2} h_j^2 \mathbf{I}_{3 \times 3} & h_j \mathbf{I}_{3 \times 3} \end{bmatrix}, \quad (23)$$

where $h_j = t_j - t_{j-1}$ is the duration of a sampling period and σ_u^2 is the diffusion coefficient to be adjusted to optimize the filter performance [31].

2. Prediction in Unscented Kalman Filter

In the UKF, the prediction involves forming and propagating $2n + 1$ sigma points, chosen as in [32],

$$\mathcal{X}_{j-1|j-1}^{(0)} = \hat{\boldsymbol{\theta}}_{j-1|j-1}, \quad (24a)$$

$$\mathcal{X}_{j-1|j-1}^{(\ell)} = \hat{\boldsymbol{\theta}}_{j-1|j-1} + \sqrt{n + \lambda} \left[\sqrt{\boldsymbol{\Sigma}_{j-1|j-1}} \right]_{\ell}, \quad \ell = 1, \dots, n, \quad (24b)$$

$$\mathcal{X}_{j-1|j-1}^{(\ell+n)} = \hat{\boldsymbol{\theta}}_{j-1|j-1} - \sqrt{n + \lambda} \left[\sqrt{\boldsymbol{\Sigma}_{j-1|j-1}} \right]_{\ell}, \quad \ell = 1, \dots, n, \quad (24c)$$

where $\left[\sqrt{\boldsymbol{\Sigma}_{j-1|j-1}} \right]_{\ell}$ corresponds to the ℓ^{th} column of the matrix square root of $\boldsymbol{\Sigma}_{j-1|j-1}$, and λ is given by

$$\lambda = \alpha^2(n + \kappa) - n. \quad (25)$$

The parameter α dictates the spread of the sigma points around the mean, usually chosen to be a small positive value, and κ is a secondary scaling parameter, usually set to 0. Each sigma point is propagated using the nonlinear dynamics

$$\mathcal{X}_{j|j-1}^{(i)} = \mathcal{X}_{j-1|j-1}^{(\ell)} + \int_{t_{j-1}}^{t_j} \mathbf{f}(\tau, \boldsymbol{\theta}(\tau)) d\tau, \quad \ell = 0, \dots, n. \quad (26)$$

Finally, the time update of the mean and the covariance are given by

$$\hat{\theta}_{j|j-1} = \sum_{\ell=0}^{2n} W_{\ell}^{(m)} \chi_{j|j-1}^{(\ell)}, \quad (27a)$$

$$\Sigma_{j|j-1} = \sum_{\ell=0}^{2n} W_{\ell}^{(c)} \left(\chi_{j|j-1}^{(\ell)} - \hat{\theta}_{j|j-1} \right) \left(\chi_{j|j-1}^{(\ell)} - \hat{\theta}_{j|j-1} \right)^T + \mathbf{Q}_j, \quad (27b)$$

where \mathbf{Q}_j is the process noise given by expression (23), while $W_i^{(m)}$ and $W_{\ell}^{(c)}$ are weights given by

$$\begin{aligned} W_0^{(m)} &= \frac{\lambda}{n + \lambda}, \\ W_0^{(c)} &= \frac{\lambda}{n + \lambda + (1 - \alpha^2 + \beta)}, \\ W_{\ell}^{(m)} &= \frac{1}{2(n + \lambda)}, \quad \ell = 1, \dots, 2n, \\ W_{\ell}^{(c)} &= \frac{1}{2(n + \lambda)}, \quad \ell = 1, \dots, 2n, \end{aligned} \quad (28)$$

and β is an additional parameter to incorporate prior knowledge of $\hat{\theta}$; $\beta = 2$ is optimal assuming the distribution of $\hat{\theta}$ is Gaussian.

3. Measurement Update

The OPNAV measurements are modeled as direct position measurements with additive Gaussian noise,

$$\mathbf{y}_j = \mathbf{E} \theta_j + \mathbf{R}_j, \quad \mathbf{R}_j \sim \mathcal{N}(\mathbf{0}, \mathbf{R}_j), \quad \mathbf{E} = \begin{bmatrix} \mathbf{I}_{3 \times 3} & \mathbf{0}_{3 \times 3} \end{bmatrix}. \quad (29)$$

The resulting linear update step of the filter is

$$\mathbf{K}_j = \Sigma_{j|j-1} \mathbf{E}^T \left(\mathbf{E} \Sigma_{j|j-1} \mathbf{E}^T + \mathbf{R}_j \right)^{-1}, \quad (30a)$$

$$\hat{\theta}_{j|j} = \hat{\theta}_{j|j-1} + \mathbf{K}_j \left(\mathbf{y}_j - \mathbf{E} \hat{\theta}_{j|j-1} \right), \quad (30b)$$

$$\Sigma_{j|j} = (\mathbf{I} - \mathbf{K}_j \mathbf{E}) \Sigma_{j|j-1} (\mathbf{I} - \mathbf{K}_j \mathbf{E})^T + \mathbf{K}_j \mathbf{R}_j \mathbf{K}_j^T, \quad (30c)$$

where the measurement \mathbf{y}_j and the measurement noise covariance \mathbf{R}_j are obtained from (9) and (13), respectively.

D. Measurement Collection for Horizon-Based Optical Navigation on Near-Rectilinear Halo Orbit

The choice of the onboard camera specifications directly impacts the number of limb points m detected within an image, and therefore the quality of the position measurement itself. Furthermore, for a given position in space, if the field of view (FOV) is too narrow and the limb of the Moon does not fit within the frame of the image, the measurement

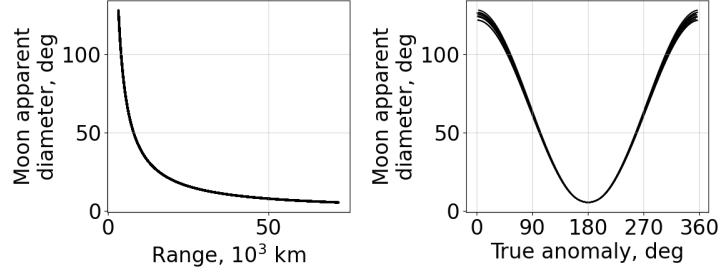


Fig. 3 Range and apparent Moon diameter against osculating true anomaly along NRHO, shown for 10 superimposed revolutions

may be unusable. The choice of camera FOV is particularly important on the NRHO due to the large variety in distance from the Moon at perilune and apolune. Figure 3 shows the range and the apparent diameter of the Moon as seen along the NRHO.

1. Effect of Field of View on Measurement

The least-squares solution of (7) is affected by the number of detected limb points m . One way to increase m may be to use a camera with a larger number of pixels on its sensor; however, this requires larger onboard processing overhead. Another tuning knob is the camera’s FOV. A camera with an FOV that exactly matches the apparent diameter of the Moon will contain the largest possible m , assuming that the Moon is exactly centered along the boresight. However, in practice, the camera is pointed to the Moon using the state estimate $\hat{\theta}$. Other operational considerations on attitude may further lead to scenarios where it is desirable to image the Moon without slewing the spacecraft too much.

2. Choice of Camera for Horizon-Based OPNAV on NRHO

For a given range from the Moon and a given level of pointing margin, the narrowest possible FOV that fits the entire limb results in the largest m , and thus the best obtainable measurement \hat{r} . However, choosing the optimal camera for a spacecraft on the NRHO is not trivial due to the large variability in range along the orbit: in the extreme case, choosing the optimal FOV at perilune will result in poor measurements at other locations along the orbit as the Moon will appear very small in the image; meanwhile, choosing the optimal FOV at apolune will not be able to image the Moon at other locations, as the range is shorter at all other locations. We can thus already hypothesize that the “best” camera will have an FOV that is suitable in some in-between ranges between perilune and apolune.

If the navigation subsystem can accommodate more than a single camera, it would be ideal to have a near-range and a far-range camera, each with FOVs suitable for different locations along the orbit. Within the scope of this work, we limit our study to a system with a single camera. As we will show with numerical results, horizon-based OPNAV measurements using an appropriately chosen FOV and taken at appropriate locations along the orbit are remarkably reliable, thus resulting in satisfactory filter and station-keeping performance.

When choosing the FOV, it is important to keep in mind that for the purpose of autonomous navigation, we seek to have reliable filter estimates near apolune, where station-keeping control maneuvers, when necessary, are executed. On one hand, there is an inherent degradation of observability as the range increases. The worsened observability is manifested in the slow variation of the Moon apparent diameter around apolune, as shown in Figure 3; as the image is taken further away from the Moon, a difference in range Δr results in a rapidly diminishing difference in the apparent diameter. The degradation of the measurement quality is reported in previous works, including Figure 9 in [4]. Meanwhile, imaging at perilune, where we have the best observability, also has its downsides: first, from an operational perspective, this may lead to pointing requirements over short periods of time to ensure the Moon is within the frame of the camera. Second, a dead-reckoning prediction from perilune until the control location near apolune may be of insufficient accuracy. Third, even if a measurement collection opportunity may arise around apolune prior to control, a camera with a sufficiently large FOV to capture the full Moon near perilune will only lead to poor measurements with a small number of limb points m near apolune. Thus, we choose an FOV sized to obtain measurements outside of regions along the orbit near perilune; to account for attitude uncertainties, we ensure the FOV is at least twice as large as the Moon's apparent diameter from where the measurement is acquired.

IV. Station-Keeping Control

There exists a multitude of controllers proposed for SK on LPOs [14]. In the context of L1 and L2 halo orbits, a popular SK controller is the so-called x -axis crossing control, which has been shown to perform well both in numerical simulations [16, 17] and in-flight [20]. A particularity about the x -axis crossing control scheme is that it has often been formulated as a multivariable root-finding problem, and rarely as a constrained minimization problem [33]. In this work, we introduce both the root-finding-based and the minimization problem-based formulations, point out their distinctions, and compare their numerical performances. Then, we propose a UT-based modification of the x -axis control that utilizes the filter's covariance estimate together with the state estimate to improve the prediction accuracy of the targeted state, and thereby reduce the cumulative ΔV .

Recent advancements in station-keeping on the NRHO also focused on tackling the phase-deviation issue associated with x -axis crossing control [19, 34]. To avoid the issue altogether, a model predictive control (MPC) scheme has also been proposed to provide full-state tracking under the same operational assumptions as x -axis crossing control [35], yielding similar cumulative ΔV and improved tracking performance. In this work, the conducted numerical experiments do not exceed ~ 400 days, and thus are minimally impacted by phase deviation. The UT-based modification proposed here is applicable to any control scheme, including x -axis crossing control schemes with phase-deviation remedies [19, 34] or the MPC in [35].

In the rest of this Section, we first provide an overview of the x -axis crossing control scheme, highlighting key findings from the literature that are relevant to our work. This is followed by a description of the root-solving-based

formulation, solved using differential correction, and the constrained minimization-based formulation.. Then, the UT-based modification, applicable to either formulation, is introduced. Finally, considerations pertaining to the control frequency and the targeting tolerance are discussed.

A. Overview of x -axis Crossing Control

The x -axis crossing control is a popular station-keeping control scheme that is widely regarded as among the most efficient, particularly for almost linearly stable periodic orbits such as the NRHO. We start with a generic optimization problem formulation that encompasses the broader family of targeting-based control and point out the specific variant that is commonly adopted in literature for the NRHO.

1. Targeting Event

Consider a spacecraft at t_0 and state estimate $\theta_0 \in \mathbb{R}^6$. The controller must bring a subset of the propagated state at time t_f , $\psi(t_f) \in \mathbb{R}^n$ where $n \leq 6$, to an n -dimensional ellipsoid from a reference target $\bar{\psi}(\bar{t}) \in \mathbb{R}^n$ at time \bar{t} , with radii $\epsilon_{j,\text{tol}}$ for $j = 0, \dots, n-1$. We denote by *targeting event* the event that defines \bar{t} . While the integration of the dynamics from time t_0 to t_f is typically done in \mathcal{F}_I , the targeted state ψ and $\bar{\psi}$ may be components in another frame \mathcal{F}_B .

In x -axis crossing control, $\bar{t} \neq t_f$, as the targeting event is not defined based on propagation time. The non-equivalence of \bar{t} and t_f is an important distinction of this control scheme compared to more conventional tracking controllers. The x -axis crossing controller gets its name from the fact that the targeting event is defined based on the time where the trajectory crosses the xz -plane near the Moon in the Earth-Moon rotating frame, \mathcal{F}_{EM} . While this does not exactly coincide with perilune, preliminary experiments have shown that the two events result in no apparent difference in the SK performance, and thus may be used interchangeably; in this work, the targeting event is defined by the perilune.

The optimal impulsive control maneuver $\mathbf{u} \in \mathbb{R}^3$ that brings the spacecraft to the n -dimensional ellipsoid centered at $\bar{\psi}(\bar{t})$ is computed by solving the nonlinear program (NLP)

$$\min_{\mathbf{u}} \quad \|\mathbf{u}\|_2, \quad (31a)$$

$$\text{such that} \quad \left| \psi^B(t_f) - \bar{\psi}^B(\bar{t}) \right| \leq v_{x,\text{tol}}, \quad (31b)$$

where the absolute value in constraint (31b) is applied component-wise. The final targeted state $\psi^B(t_f)$ is the subset of the propagated state at t_f , $\theta^B(t_f)$, transformed from the inertial frame to frame \mathcal{F}_B , obtained by propagating the nonlinear dynamics with control \mathbf{u} ,

$$\theta^B(t_f) = T_B^{\text{Inr}} \left(\theta_0 + \begin{bmatrix} \mathbf{0}_{3 \times 3} \\ I_3 \end{bmatrix} \mathbf{u} + \int_{t_0}^{t_f} \mathbf{f}[\tau, \theta] d\tau \right), \quad (32)$$

where $T_B^{\text{Inr}} \in \mathbb{R}^{6 \times 6}$ is the transformation matrix from \mathcal{F}_I to \mathcal{F}_B .

Instead of targeting the immediate perilune, it is common to choose the N^{th} perilune downstream with $N > 1$ to improve the ΔV performance, subject to the reliability of the predicted state affected by estimation, dynamics, and control execution errors. In this work, $N = 7$ is adopted in accordance to previous results on the NRHO [17, 19].

Finally, the n state components to target, the frame in which these state components are represented, and the tolerance on the tightness of the targeting, must be chosen. Previous works have successfully demonstrated that targeting the x -component velocity in \mathcal{F}_{EM} , denoted hereafter by v_x^{EM} , is sufficient for tracking a baseline NRHO trajectory under reasonable levels of errors and uncertainties [16, 17, 19]. Following their definition, \mathcal{F}_B is \mathcal{F}_{EM} , and $\psi^B = v_x^{\text{EM}}$. Then, constraint (31b) is actually

$$|v_x^{\text{EM}}(t_f) - \bar{v}_x^{\text{EM}}(\bar{t})| \leq v_{x,\text{tol}}, \quad (33)$$

where $v_x^{\text{EM}}(t_f)$ is part of the final state $\theta^{\text{EM}}(t_f)$ obtained by transforming the solution to the initial value problem (32), and $\bar{v}_x^{\text{EM}}(\bar{t})$ is reference x -axis velocity in the instantaneous \mathcal{F}_{EM} at the targeted perilune. One may interpret the x -axis crossing controller using v_x^{EM} alone as tracking only the state components necessary for stabilizability. The effect of the tolerance on v_x^{EM} has been investigated by Guzzetti et al. [17] using deep space network-based orbit determination, but it is revisited in this work to highlight the controller's interplay with horizon-based OPNAV.

2. Control Location Selection

The control location along the NRHO is parameterized in terms of the instantaneous true anomaly, as shown in Figure 4. The particularly high sensitivity of the dynamics near perilune on the NRHO makes this region sensitive to errors, and is usually considered unsuitable for station-keeping [17]; thus, the control maneuver is to be located at or near the apolune, at a true anomaly of around 180° . Guzzetti et al. [17] previously provided results demonstrating a relatively low sensitivity of the maneuver placement at true anomalies between about 160° and 200° on the cumulative yearly station-keeping cost. For example, the Gateway's station-keeping strategy incorporates a single maneuver at 200° [19], driven by the aforementioned reasons as well as operational considerations. We define the *control action true anomaly* as the true anomaly about which the controller evaluates the need for control, and if needed, computes the required maneuver, to study its impact on the SK cost for a navigation based on OPNAV.

B. x -axis Crossing Control via Differential Correction

A common solution approach for solving (31) adopted in the literature [16, 17, 19, 36] is differential correction (DC), which involves recasting (31) as an under-determined root-finding problem with a shooting function $F : \mathbb{R}^3 \rightarrow \mathbb{R}$,

$$F(\mathbf{u}) = v_x^{\text{EM}}(t_f) - \bar{v}_x^{\text{EM}}(\bar{t}), \quad (34)$$

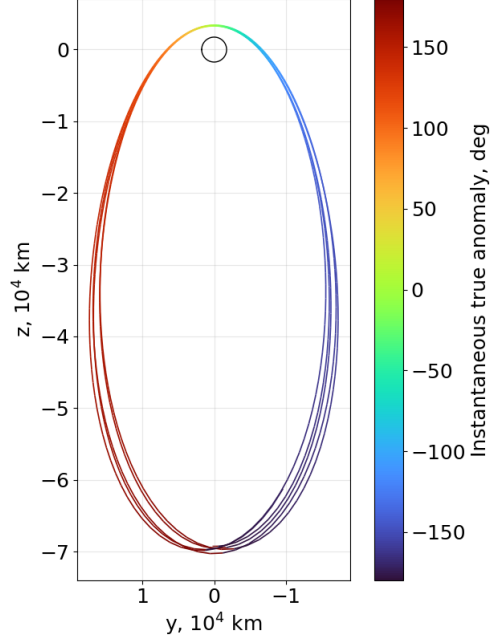


Fig. 4 NRHO shown with instantaneous true anomaly for 10 revolutions, seen from the near-side of the Moon (Earth-side observer) in the Earth-Moon rotating frame. In this view, the spacecraft tracks the orbit anti-clockwise.

seeking $F(\mathbf{u}) = 0$. Employing an iterative scheme such as a generalized Newton-Raphson method, one may employ the minimum-norm update given at the i^{th} iteration

$$\mathbf{u}^{(i+1)} = \mathbf{u}^{(i)} - \left(\frac{\partial F(\mathbf{u}^{(i)})}{\partial \mathbf{u}} \right)^T \left[\left(\frac{\partial F(\mathbf{u}^{(i)})}{\partial \mathbf{u}} \right)^T \left(\frac{\partial F(\mathbf{u}^{(i)})}{\partial \mathbf{u}} \right) \right]^{-1} F(\mathbf{u}^{(i)}), \quad (35)$$

where $\partial F / \partial \mathbf{u}$ is the Jacobian. Since \mathbf{u} is essentially a perturbation on the initial velocity $\delta \mathbf{v}_0$, this Jacobian can be computed from the STM as

$$\frac{\partial F}{\partial \mathbf{u}} = \left(T_{\text{EM}}^{\text{Inr}} \begin{bmatrix} \Phi_{rv}(t_f, t_0) \\ \Phi_{vv}(t_f, t_0) \end{bmatrix} \right)_{[4,:]} = \left(T_{\text{EM}}^{\text{Inr}} \Phi_{[:,4:6]}(t_f, t_0) \right)_{[4,:]}, \quad (36)$$

where $\Phi_{[:,4:6]}$ is the last three columns of the STM and $(\cdot)_{[4,:]}$ denotes the fourth row of the matrix. While a DC-based approach does not directly minimize the control effort, it still yields adequate performance as the minimum-norm update (35) promotes successive updates from $\mathbf{u}^{(i)}$ to $\mathbf{u}^{(i+1)}$ to be as small as possible. Nevertheless, DC does not guarantee that the root-finding process will converge to \mathbf{u}^* that satisfies (33) with the smallest possible magnitude. Instead, DC can results in “over-compensating” for the residual $F(\mathbf{u})$ by returning a control that brings $F(\mathbf{u}) \rightarrow 0$ with its quadratic convergence nature. The popularity of DC is attributed to its resemblance to the procedure used for

trajectory design, with the only difference being the choice of the targeted state $\psi(t_f)$. The overall DC process is shown in Algorithm 1 where the function `sxform` constructs the transformation matrix from \mathcal{F}_1 to \mathcal{F}_{EM} at time t_f , and the function `SolveIVPSTM`($t_0, t_f, \theta_0 + \text{vec}(\mathbf{0}_{3 \times 1}, \bar{\mathbf{u}})$) solves the IVP for the initial state $\theta_0 + \text{vec}(\mathbf{0}_{3 \times 1}, \bar{\mathbf{u}})$ and the STM from time t_0 to t_f by integrating the nonlinear dynamics and the matrix differential equation (4).

Algorithm 1 x -axis crossing control via differential correction

Require: $t_0, \theta_0, t_f, \bar{v}_x^{\text{EM}}, v_{x,\text{tol}}, \text{maxiter}$
 $T_{\text{EM}}^{\text{Inr}} \leftarrow \text{sxform}(t_f)$
 $\mathbf{u} \leftarrow \mathbf{0}_{3 \times 1}$ ▷ Initialize cumulative control vector
for iter = 1, ..., maxiter **do**
 $\theta_{f,0}, \Phi(t_f, t_0) \leftarrow \text{SolveIVPSTM}(t_0, t_f, \theta_0 + \text{vec}(\mathbf{0}_{3 \times 1}, \bar{\mathbf{u}}))$
if $|v_{x,0}^{\text{EM}}(t_f) - \bar{v}_x^{\text{EM}}| \leq v_{x,\text{tol}}$ **then** ▷ Check if nonlinear targeting constraint is cleared
 break
end if
 $F \leftarrow v_{x,0}^{\text{EM}}(t_f) - \bar{v}_x^{\text{EM}}$
 $DF \leftarrow (T_{\text{EM}}^{\text{Inr}} \Phi[:, 4:6](t_f, t_0))_{[4,:]}$
 $\mathbf{u} \leftarrow \mathbf{u} - DF^T (DF^T DF)^{-1} F$ ▷ Minimum-norm update
end for
return \mathbf{u}

C. x -axis Crossing Control as a Sequentially Linearized Minimization Problem

Alternatively, (31) can be solved through sequential linearization. Specifically, we replace the IVP (32) with linearization

$$\theta^{\text{EM}}(t_f) = T_{\text{EM}}^{\text{Inr}} \left(\int_{t_0}^{t_f} f(\tau, \theta_0) d\tau + \begin{bmatrix} \Phi_{rv}(t_f, t_0) \\ \Phi_{vv}(t_f, t_0) \end{bmatrix} \mathbf{u} \right) = T_{\text{EM}}^{\text{Inr}} \theta_{f,0} + B\mathbf{u}, \quad (37)$$

where $\theta_{f,0}$ is the final state at t_f if no control is executed at t_0 , and

$$B = T_{\text{EM}}^{\text{Inr}} \begin{bmatrix} \Phi_{rv}(t_f, t_0) \\ \Phi_{vv}(t_f, t_0) \end{bmatrix} = T_{\text{EM}}^{\text{Inr}} \Phi[:, 4:6](t_f, t_0). \quad (38)$$

Then, denoting $v_{x,0}^{\text{EM}}(t_f) = (T_{\text{EM}}^{\text{Inr}} \theta_{f,0})_{[4]}$, the linearized problem is given by

$$\min_{\mathbf{u}} \quad \|\mathbf{u}\|_2 \quad (39a)$$

$$\text{such that} \quad |v_{x,0}^{\text{EM}}(t_f) + B_{[4,:]} \mathbf{u} - \bar{v}_x^{\text{EM}}| \leq v'_{x,\text{tol}}, \quad (39b)$$

where $(\cdot)_{[4]}$ denotes the fourth component of the vector. The constraint (39b) is bounded by $v'_{x,\text{tol}}$, which is given in terms of the original targeting tolerance $v_{x,\text{tol}}$ by $v'_{x,\text{tol}} = s v_{x,\text{tol}}$ where $0 < s < 1$ is a safety factor set to $s = 0.9$ in this

work. Setting $v'_{x,\text{tol}} < v_{x,\text{tol}}$ ensures the actual nonlinear constraint (39b) is achieved by sequentially updating \mathbf{u} with the solution of the linearized problem (39).

Solving the *minimization* problem (39) is different from solving the root-finding problem (34) in two regards. First, the dynamics have been linearized using the STM in (37). Thus, the obtained solution \mathbf{u} may not satisfy the constraint when propagated with the nonlinear IVP (32). In SK, the control that is sought is typically small in magnitude, and the linear approximation holds relatively well. Nevertheless, a few iterations ($2 \sim 3$ in practice) solving (39) by updating $\theta_{f,0}$ and B may be necessary to incrementally obtain an aggregate control $\bar{\mathbf{u}}$ and satisfy the nonlinear constraint (33). Specifically, after the i^{th} iteration solving the linearized problem, $\theta_{f,0}$ is replaced by $\theta_{f,0} \leftarrow \theta_{f,0} + \mathbf{u}^{(i)}$ where $\mathbf{u}^{(i)}$ is the solution from the i^{th} iteration, and B is reconstructed using the updated initial state for the $i + 1^{\text{th}}$ iteration. Second, because this is a minimization of $\|\mathbf{u}\|_2$, the resulting control \mathbf{u} is the minimum feasible \mathbf{u} that simultaneously ensures the final v_x^{EM} to be within $v'_{x,\text{tol}}$ of the targeted value \bar{v}_x^{EM} according to the linear approximated dynamics (37).

Problem (39) is a SOCP, where the Euclidean norm in the objective may be formulated as a second-order cone constraint. Its optimal solution may be obtained analytically by observing that it is equivalent to determining the projection of the origin to the intersection of two half-spaces [22]. The control \mathbf{u} satisfying (39b) is a vector \mathbf{y} that belongs to the intersection of two half-spaces given by

$$\begin{aligned} C &= \left\{ \mathbf{y} \mid B_{[4,:]} \mathbf{y} \leq v'_{x,\text{tol}} - v_{x,0}^{\text{EM}}(t_f) + \bar{v}_x^{\text{EM}} \right\} \cap \left\{ \mathbf{y} \mid -B_{[4,:]} \mathbf{y} \leq v'_{x,\text{tol}} + v_{x,0}^{\text{EM}}(t_f) - \bar{v}_x^{\text{EM}} \right\}, \\ &= \left\{ \mathbf{y} \mid \xi_1^T \mathbf{y} \leq \eta_1 \right\} \cap \left\{ \mathbf{y} \mid \xi_2^T \mathbf{y} \leq \eta_2 \right\}, \end{aligned} \quad (40)$$

where

$$\xi_1^T = B_{[4,:]}, \quad (41)$$

$$\xi_2^T = -B_{[4,:]}, \quad (42)$$

$$\eta_1 = v'_{x,\text{tol}} - v_{x,0}^{\text{EM}}(t_f) + \bar{v}_x^{\text{EM}}, \quad (43)$$

$$\eta_2 = v'_{x,\text{tol}} + v_{x,0}^{\text{EM}}(t_f) - \bar{v}_x^{\text{EM}}. \quad (44)$$

The expression for the projection of \mathbf{y} onto C is given by Proposition 28.19 in [37]

$$P_C \mathbf{y} = \mathbf{y} - \nu_1 \xi_1 - \nu_2 \xi_2, \quad (45)$$

where exactly one of the following holds:

$$\begin{aligned} \begin{bmatrix} v_1 \\ v_2 \end{bmatrix} = \begin{cases} \begin{bmatrix} 0 \\ 0 \end{bmatrix} & \xi_1^T \mathbf{y} \leq \eta_1 \text{ and } \xi_2^T \mathbf{y} \leq \eta_2, \\ \begin{bmatrix} \frac{\|\xi_2\|^2(\mathbf{y}^T \xi_1 - \eta_1) - \xi_1^T \xi_2(\mathbf{y}^T \xi_2 - \eta_2)}{\|\xi_1\|^2 \|\xi_2\|^2 - |\xi_1^T \xi_2|^2} \\ \frac{\|\xi_1\|^2(\mathbf{y}^T \xi_2 - \eta_2) - \xi_1^T \xi_2(\mathbf{y}^T \xi_1 - \eta_1)}{\|\xi_1\|^2 \|\xi_2\|^2 - |\xi_1^T \xi_2|^2} \end{bmatrix} & \|\xi_2\|^2(\mathbf{y}^T \xi_1 - \eta_1) > \xi_1^T \xi_2(\mathbf{y}^T \xi_2 - \eta_2) \text{ and} \\ & \|\xi_1\|_2(\mathbf{y}^T \xi_2 - \eta_2) > \xi_1^T \xi_2(\mathbf{y}^T \xi_1 - \eta_1), \\ \begin{bmatrix} 0 \\ \frac{\mathbf{y}^T \xi_2 - \eta_2}{\|\xi_2\|^2} \\ \frac{\mathbf{y}^T \xi_1 - \eta_1}{\|\xi_1\|^2} \\ 0 \end{bmatrix} & \mathbf{y}^T \xi_2 > \eta_2 \text{ and} \\ & \|\xi_2\|^2(\mathbf{y}^T \xi_1 - \eta_1) \leq \xi_1^T \xi_2(\mathbf{y}^T \xi_2 - \eta_2), \\ & \mathbf{y}^T \xi_1 > \eta_1 \\ & \text{and } \|\xi_1\|^2(\mathbf{y}^T \xi_2 - \eta_2) \leq \xi_1^T \xi_2(\mathbf{y}^T \xi_1 - \eta_1). \end{cases} \end{aligned} \quad (46)$$

Since we seek to minimize $\|\mathbf{u}\|_2$, choosing $\mathbf{y} = \mathbf{0}_{3 \times 1}$ in equation (45) yields the optimal solution $\mathbf{u}^* = P_C \mathbf{0}_{3 \times 1}$ to problem (39).

In summary, the sequential linearization approach solves the NLP (31) by sequentially building the linearized problem (39) and computing its solution via (45). The overall procedure is termed the “sequentially linearized minimization problem” (SLMP), and is summarized in Algorithm 2, where the function `sxform` forms the transformation matrix at time t_f , and the function `OriginProjectionCoefficients` computes the coefficients v_1 and v_2 with $\mathbf{y} = \mathbf{0}_{3 \times 1}$ using equation (46). The algorithm returns the aggregated control vector $\bar{\mathbf{u}}$, which is the summation of the solution \mathbf{u} of each sequential instance of the linearized problem (39).

Algorithm 2 x -axis crossing control via sequentially linearized minimization problem

Require: $t_0, \theta_0, t_f, \bar{v}_x^{\text{EM}}, v_{x,\text{tol}}, s, \text{maxiter}$

$v'_{x,\text{tol}} \leftarrow s v_{x,\text{tol}}$

$T_{\text{EM}}^{\text{Inr}} \leftarrow \text{sxform}(t_f)$

$\bar{\mathbf{u}} \leftarrow \mathbf{0}_{3 \times 1}$

► Initialize cumulative control vector

for $\text{iter} = 1, \dots, \text{maxiter}$ **do**

$\theta_{f,0}, \Phi(t_f, t_0) \leftarrow \text{SolveIVPSTM}(t_0, t_f, \theta_0 + \text{vec}(\mathbf{0}_{3 \times 1}, \bar{\mathbf{u}}))$

if $\left| v_{x,0}^{\text{EM}}(t_f) - \bar{v}_x^{\text{EM}} \right| \leq v_{x,\text{tol}}$ **then**
break

► Check if nonlinear targeting constraint is cleared

end if

$B \leftarrow T_{\text{EM}}^{\text{Inr}} \Phi_{[:,4:6]}(t_f, t_0)$

$\eta_1, \xi_1, \eta_2, \xi_2 \leftarrow \text{equations (41) } \sim \text{ (44)}$

$v_1, v_2 \leftarrow \text{OriginProjectionCoefficients}(\eta_1, \xi_1, \eta_2, \xi_2)$

► Via equation (46)

$\mathbf{u} \leftarrow -v_1 \xi_1 - v_2 \xi_2$

► Compute linearized control update

$\bar{\mathbf{u}} \leftarrow \bar{\mathbf{u}} + \mathbf{u}$

► Update cumulative control vector

end for

return $\bar{\mathbf{u}}$

D. Mean State Targeting via Unscented Transform

Traditional x -axis crossing control introduced thus far involves targeting the state $\psi(t_f)$, obtained by simply propagating the current state estimate. The resulting predicted state $\psi(t_f)$ may be understood as the prediction output from the EKF, where the best estimate of a future state is obtained by propagating the current state estimate forward in time. While filter performance for navigation have resulted in no apparent difference between EKF and UKF, the state prediction involved in control is over a significantly longer time, across multiple revolutions along the periodic orbit. Thus, a UT-based prediction can better capture the nonlinearity involved. Hence, we consider a control scheme which aims at steering the mean future state $\mathbb{E}[\psi^B(t_f)]$ computed via the unscented transform. The resulting NLP is given by

$$\min_{\mathbf{u}} \quad \|\mathbf{u}\|_2, \quad (47a)$$

$$\text{such that} \quad \left| \mathbb{E}[\psi^B(t_f)] - \bar{\psi}^B \right| \leq v_{x,\text{tol}}, \quad (47b)$$

The mean targeted state $\mathbb{E}[\psi^B(t_f)]$ under no control maneuver can be approximated using the unscented transform, as in the prediction step of the UKF (27a). The mean predicted state at time t_f is approximated by

$$\mathbb{E}[\psi_0^{\text{EM}}(t_f)] \approx \left(\sum_{\ell=0}^{2n} W_m^{(\ell)} \mathcal{Y}^{(\ell)} \right)_m, \quad (48)$$

where \mathcal{Y}^ℓ is given by

$$\mathcal{Y}^\ell = T_{\text{EM}}^{\text{Inr}} \left(X_{j-1|j-1}^{(\ell)} + \int_{t_{j-1}}^{t_j} f(\tau, X_{j-1|j-1}^{(\ell)}(\tau)) d\tau \right), \quad \ell = 0, \dots, n, \quad (49)$$

with sigma points computed by (24). By replacing $v_x^{\text{EM}}(t_f)$ in (34) or $v_{x,0}^{\text{EM}}(t_f)$ in (39b) with $\mathbb{E}[\psi_0^{\text{EM}}(t_f)]$, both the DC and SLMP approaches are modified to target the mean state, and are referred to as UT-DC and UT-SLMP, respectively.

The intuition behind the expected performance improvement by solving problem (47) instead of (31) is due to the improvement of the prediction accuracy that we obtain by capitalizing on the filter's covariance estimate. The initial state estimate error, propagated over targeting time t_f spanning multiple weeks, is more effectively countered by also propagating the sigma points from the initial covariance.

E. Trigger Condition and Targeting Tolerance Tuning

At each control action true anomaly, a trigger condition is used to determine whether a SK maneuver should be executed. Such a condition necessitates an indicator that quantifies the difference of the state estimate from the baseline. For the x -axis crossing control, a typical indicator is the difference in magnitude of v_x^{EM} at the N^{th} perilune with respect to the baseline. We define the threshold $v_{x,\text{trig}}$ such that a control is triggered if $|v_x^{\text{EM}} - \bar{v}_x^{\text{EM}}| \geq v_{x,\text{trig}}$. While both the

DC and SLMP approaches use this dead-band $v_{x,\text{trig}}$, the SLMP approach also requires appropriately tuning $v_{x,\text{tol}}$.

When employing DC, the actual targeting violation $|v_x^{\text{EM}} - \bar{v}_x^{\text{EM}}|$ achieved is somewhat uncorrelated to $v_{x,\text{tol}}$ due to the quadratic convergence nature; as such, the DC algorithm most often converges $|v_x^{\text{EM}} - \bar{v}_x^{\text{EM}}| \ll v_{x,\text{tol}}$. Thus, as long as an appropriate $v_{x,\text{trig}}$ is chosen, setting $v_{x,\text{tol}}$ plays a relatively small role. The arguably arbitrary nature of the DC converging at different levels of $|v_x^{\text{EM}} - \bar{v}_x^{\text{EM}}|$ is an inherent hysteresis mechanism.

In contrast, the SLMP constrained minimization problem consistently aims at achieving $|v_x^{\text{EM}} - \bar{v}_x^{\text{EM}}| = v_{x,\text{tol}}$ to minimize the control action. As such, $v_{x,\text{tol}}$ plays a concrete role in determining how well the controller tracks the baseline. A tight $v_{x,\text{tol}}$ results in expending more control effort to align the path closely to the baseline, while a relaxed $v_{x,\text{tol}}$ results in the opposite behavior.

V. Filter Experiments

The first numerical experiment consists of running the synthetic image generation, processing it to generate position measurements, which are then fed to the recursive navigation filter. Results in this section do not include the station-keeping controller and focus on the performance of the filter alone. Without a controller, the trajectory naturally diverges after several revolutions due to the accumulation of numerical integration errors. As such, a simulation experiment without a controller can only last a limited number of revolutions. Meanwhile, the filter's performance can be assessed within a few revolutions as the illumination conditions on an NRHO are almost periodic, and measurement qualities from one revolution to the next are nearly identical. Thus, in this section, for each considered filter configuration, 30 Monte-Carlo samples each lasting 10 revolutions are taken. The initial baseline epoch and state are given in Table 2. Across each Monte-Carlo run, the initial state estimate is computed by adding a random initial injection error of $3\sigma_r = 10$ km and $\sigma_v = 10$ cm/s to the baseline's initial state. At each measurement instance, the camera is pointed toward the Moon based on the current state estimate; due to the estimation error, the boresight never exactly aligns with the center of the Moon.

We consider 12 measurement collection policies in total, summarized in Table 4. To abide by the typical operational requirement of a spacecraft, it is desirable to limit the number of measurements for navigational updates to a reasonably small number and low frequency. After initial investigations, we have found that taking a small number of images around the apolune region prior to the control is able to yield satisfactory navigation performance for station-keeping. Thus, we consider 3 and 4 measurement collection policies, where 2 or 3 measurements are taken before apolune in anticipation of a station-keeping maneuver, and one measurement is taken after such a maneuver and prior to the next perilune. For each case, the FOV is chosen so that an object with twice the apparent diameter of the Moon fits within the frame of the image at the closest range where a measurement is to be taken. For example, when collecting measurements at true anomalies of 140° , 150° , and 220° , the closest measurement occurs at a true anomaly of 140° or 220° . While beyond the scope of this current work, one may choose to further optimize both the choice of the FOVs and the locations where

Table 2 Baseline initial epoch and state in Moon-centered J2000

Baseline parameter	Value
Epoch, seconds past J2000	946728069.183919
x , km	-100.3227942169551
y , km	17287.240158966662
z , km	-68230.31701814539
v_x , km/s	-0.05947862362245673
v_y , km/s	0.03798023721969298
v_z , km/s	0.005508556661896624

Table 3 Parameters and errors considered in filter experiments

Parameter and error	Value
Canonical length LU , km	3000.0
Canonical time TU , s	2346.711856601253
Process noise diffusion coefficient σ_u	1.5
Initial 3- σ position error, km	10
Initial 3- σ velocity error, cm/s	10
Attitude uncertainty σ_ϕ , arcsec	15
Pixel standard deviation σ_{pix}	0.5
SRP A/m relative uncertainty $\sigma_{A/m}$	0.1
SRP C_r relative uncertainty σ_{C_r}	0.05

the measurements are collected, but we focus on providing a sense of the trade-off that is in question.

A. Trade-off on Measurement Collection

Figure 5 shows the distribution of measurement errors for each FOV choice, taken at the three respective osculating true anomaly positions along the NRHO. Each histogram contains 300 samples in total, coming from measurements collected over 10 revolutions in each of the 30 Monte-Carlo runs. Due to the choice of the measurement collection strategy that is symmetric in true anomaly about the apolune, the first and third measurements share very similar quality, with similar distribution of measurement errors. In contrast, the second measurement is always the worst, since it is taken further away than the first or third measurement, resulting in smaller number of limb points m detected, and therefore used, in the Christian-Robinson algorithm.

The difference between the second versus the first and last measurements is least pronounced for the case with the largest FOV, as the difference in range between the measurements is the smallest; in contrast, with the smallest FOV, the difference in range is the most pronounced, thus resulting in not only the worst, but also the largest degradation between the first/last and the second measurement.

Table 4 Measurement Collection Configurations. All configurations considers a square sensor of size 100×100 mm.

Focal length	Field of view, deg	Number of measurements	Measurement true anomaly, deg
300	18.92	3	140, 150, 220
		4	140, 145, 150, 220
360	15.81	3	145, 155, 215
		4	145, 150, 155, 215
450	12.68	3	150, 160, 210
		4	150, 155, 160, 210
550	10.39	3	155, 165, 205
		4	155, 160, 165, 205

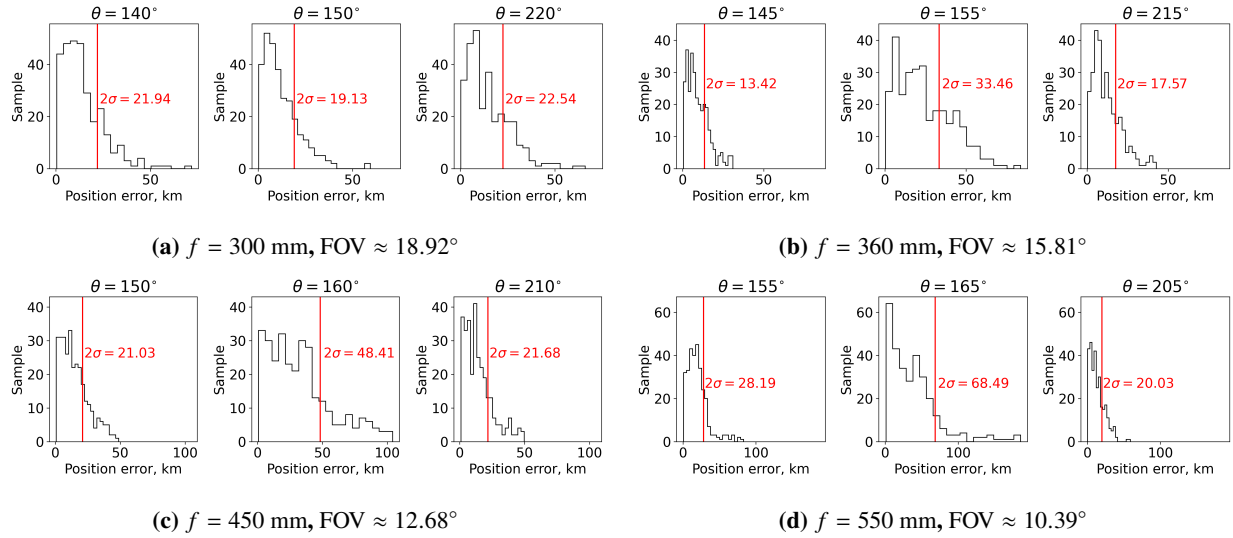


Fig. 5 Measurement statistics for various camera FOV choices

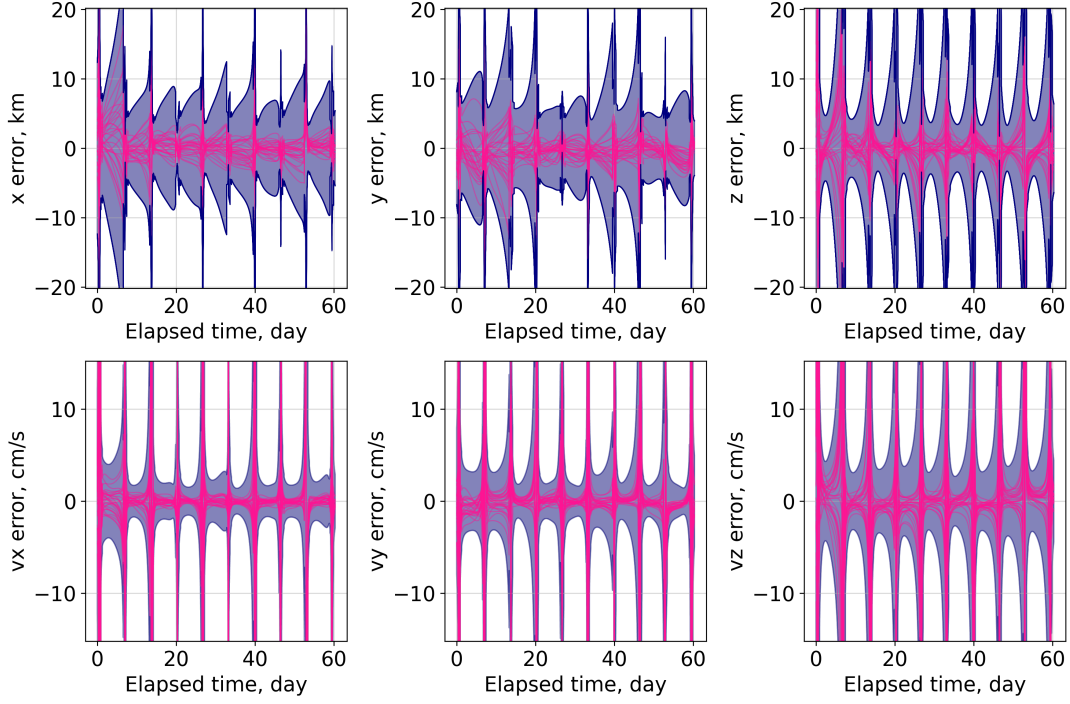


Fig. 6 EKF performance with 3 measurements per revolution, $f = 360$ mm camera, for 30 Monte-Carlo runs; dark blue shaded region corresponds to $3\text{-}\sigma$.

B. EKF Performance

With the measurement configurations in Table 4, the EKF is able to track the state estimate without diverging/wrongfully converging. As an illustrative example, the EKF performance using a $f = 360$ mm camera is shown in Figure 6. While each run is randomized in terms of initial state error, error on the SRP coefficients of the true dynamics, and attitude error, the measurement itself is taken at locations within tens of kilometers difference from one Monte-Carlo run to another; thus, for any i^{th} measurement during a Monte-Carlo run, the analytical measurement covariance from equation (13) is nearly identical to that of the i^{th} measurement in any other Monte-Carlo run.

The difference in performance between each measurement configuration is visualized through the filter's diagonal standard deviation history, shown against true anomaly ranges around apolune across the 10 revolutions in Figures 7 through 10. The red vertical lines indicate measurements, where the standard deviation sees a discrete drop due to the Kalman update. The standard deviation in velocity, which is of particular interest for station-keeping, follows a local minima that falls in the vicinity of apolune, but its exact location varies. Measurements with $f = 300$ mm or $f = 360$ mm result in lower v_z standard deviation; $f = 360$ mm also sees slight improvement in standard deviations in v_x and v_y , and is thus chosen as the measurement collection configuration for the GNC pipeline experiments in Section VII. While beyond the scope of this investigation, this experiment highlights the potential benefit of further optimizing and fine-tuning the camera FOV or measurement collection location and frequency for a specific orbit.

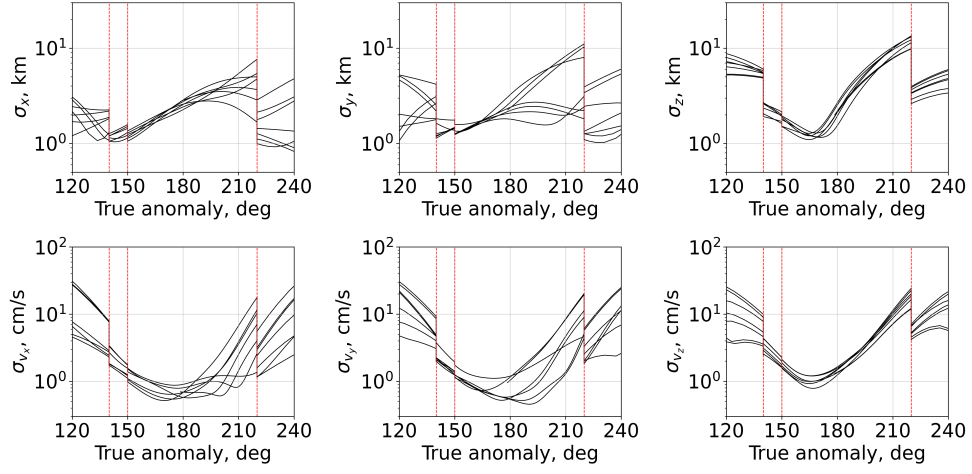


Fig. 7 EKF filter standard deviation with 3 measurements per revolution, $f = 300$ mm camera. Red dashed lines indicate measurement collection.

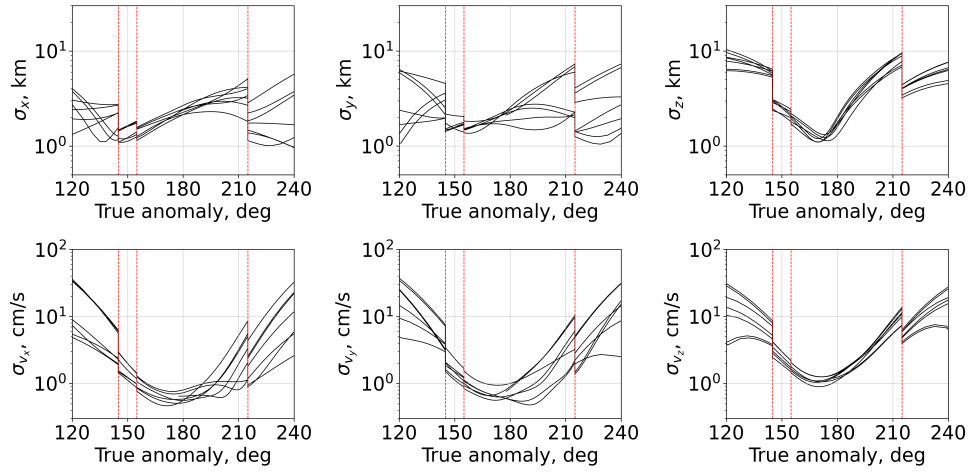


Fig. 8 EKF filter standard deviation with 3 measurements per revolution, $f = 360$ mm camera. Red dashed lines indicate measurement collection.

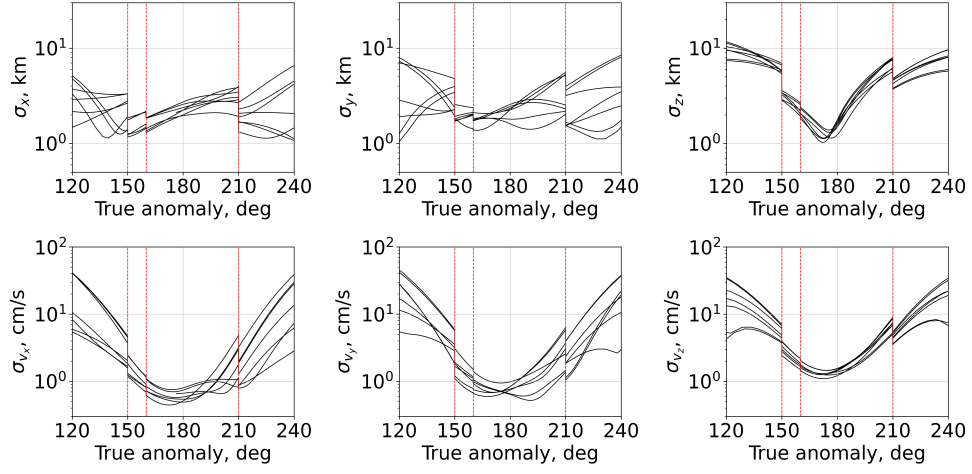


Fig. 9 EKF filter standard deviation with 3 measurements per revolution, $f = 450$ mm camera. Red dashed lines indicate measurement collection.

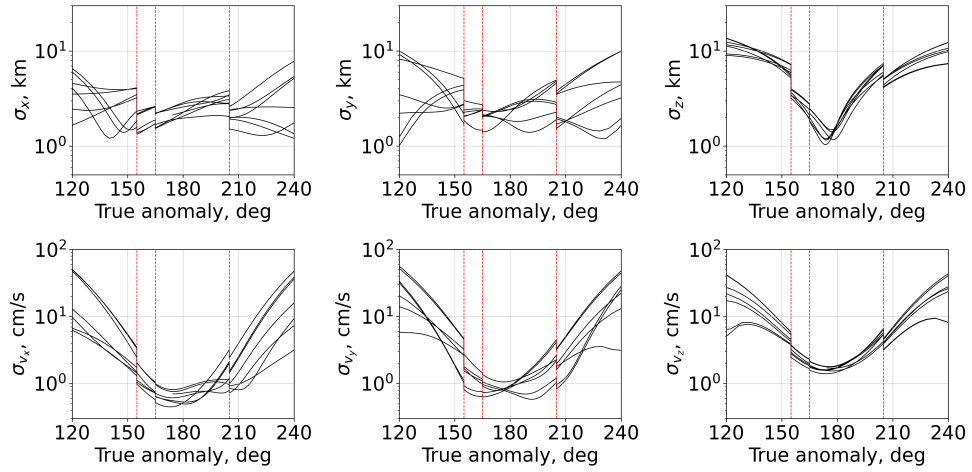


Fig. 10 EKF filter standard deviation with 3 measurements per revolution, $f = 550$ mm camera. Red dashed lines indicate measurement collection.

Table 5 Errors considered in controller experiments

Sources of error	3- σ values
Initial position error, km	10
Initial velocity error, cm/s	10
Orbit determination position error, km	5
Orbit determination velocity error, cm/s	5
Control magnitude, relative	0.03
Control direction, deg	1.5
SRP A/m , relative	0.3
SRP C_r , relative	0.15

Table 6 Summary of 100 Monte-Carlo samples targeting v_x with $3\text{-}\sigma_r = 5$ km and $3\text{-}\sigma_v = 3$ cm/s

Case	Controller	$v_{x,\text{trig}}$, m/s	$v_{x,\text{tol}}$, m/s	Success rate	Iteration	Mean yearly cost, cm/s	95 th percentile yearly cost, cm/s	Max yearly cost, cm/s
1A	DC	10	10	100%	1.89	83.8773	115.1519	130.4022
		20	20	100%	1.62	83.8494	114.7258	129.0716
		30	30	100%	1.42	85.4544	120.8226	130.8868
1B	DC	10	1	100%	2.31	82.8235	107.5520	124.5990
		20	1	100%	2.14	83.4813	109.2116	128.2814
		30	1	100%	2.04	88.2740	125.7852	141.7324
1C	SLMP	10	10	100%	2.17	105.5514	153.9997	187.8461
		20	20	100%	2.11	149.8774	190.8868	200.1280
		30	30	100%	2.07	194.1635	230.0571	247.6634
1D	SLMP	10	1	100%	2.45	84.2067	117.9776	129.9781
		20	1	100%	2.25	84.8724	114.3384	133.6056
		30	1	100%	2.12	90.4282	121.6698	147.0017

VI. Controller Experiments

Prior to running the full GNC pipeline, a control-only experiment is run. The purpose of experimenting only with the controller is to efficiently evaluate a large variety of strategies and controller tuning. We study the use of DC versus the SLMP, mean state targeting via UT, and hysteresis via trigger condition and targeting tolerance tuning. The navigation error is drawn from a Gaussian distribution with position and velocity standard deviations of $3\text{-}\sigma_r = 5$ km and $3\text{-}\sigma_v = 3$ cm/s; these values are chosen as conservative estimations that can be achieved with OPNAV based on the filter experiment with $f = 360$ mm and 3 measurements per revolution. For each controller configuration, 100 Monte-Carlo samples are taken, each lasting 60 NRHO revolutions, corresponding to about 393 days, using the same baseline NRHO as in Section V. In all cases considered within this experiment, the SK maneuver is executed at a true anomaly of 180° . The various sources of error considered along with their $3\text{-}\sigma$ values are given in Table 5.

Table 7 Summary of 100 Monte-Carlo samples targeting UT-based $\mathbb{E}[v_x]$ with $3\text{-}\sigma_r = 5$ km and $3\text{-}\sigma_v = 3$ cm/s

Case	Controller	$v_{x,\text{trig}}$, m/s	$v_{x,\text{tol}}$, m/s	Success rate	Iteration	Mean yearly cost, cm/s	95 th percentile yearly cost, cm/s	Max yearly cost, cm/s
2A	UT-DC	10	1	100%	2.54	77.4864	97.9576	104.2412
		20	1	100%	2.29	76.7389	96.8750	106.5511
		30	1	100%	2.06	82.4126	108.1957	138.7464
2B	UT-SLMP	10	1	100%	3.18	77.3861	100.2806	119.0069
		20	1	100%	2.84	77.7389	103.6512	116.1897
		30	1	100%	2.57	81.8755	112.0431	123.8050

A. Comparison of Differential Correction against SLMP

We first focus on the difference in performance between DC and SLMP, without and with hysteresis. Table 6 summarizes the statistics from the Monte-Carlo runs, and Figure 11 shows the distribution of the achieved violation of v_x after control on the top row, and the yearly cost on the bottom row.

First, we observe by comparing cases 1A and 1B that the DC without or with hysteresis perform similarly; in contrast, looking at cases 1C and 1D, SLMP performs significantly worse than the other three cases when hysteresis is not used. The need for hysteresis is apparent by the top row in Figure 11, where the achieved v_x violations between 1A and 1B are similar, and starkly different between 1C and 1D; in cases 1A, 1B and 1D a tight v_x violation is achieved, while in 1C, the minimization problem aims to satisfy the targeting constraint at a higher tolerance, thus resulting in a higher cumulative cost.

B. Efficacy of UT-Mean State Targeting

We now compare the use of unscented transform. Table 7 summarizes the statistics from the Monte-Carlo runs. Figure 12 shows the distribution of the achieved violation of v_x after control on the top row, and the yearly cost on the bottom row. Comparing 2A against 1B and 2B against 1D, we see that the use of UT improves the performance for both the DC and SLMP approach. This improvement validates the motivation of the UT-based approach: the effect of the errors on the initial state estimate is attenuated by incorporating sigma points to predict the final targeted state. The use of UT results in an increase in the average number of iterations required, as the problem is capturing the nonlinearity better, and both DC and SLMP are based on linearized correction schemes or dynamics, respectively.

VII. GNC Pipeline Validation

The final set of numerical experiments consists of validating the entire pipeline, with online generation of synthetic images, simulation of onboard navigation filtering, and station-keeping. Building upon the insights from Section V, we select a camera with $f = 360$ mm, taking measurements at true anomalies of 145° , 155° , and 215° . We test controller

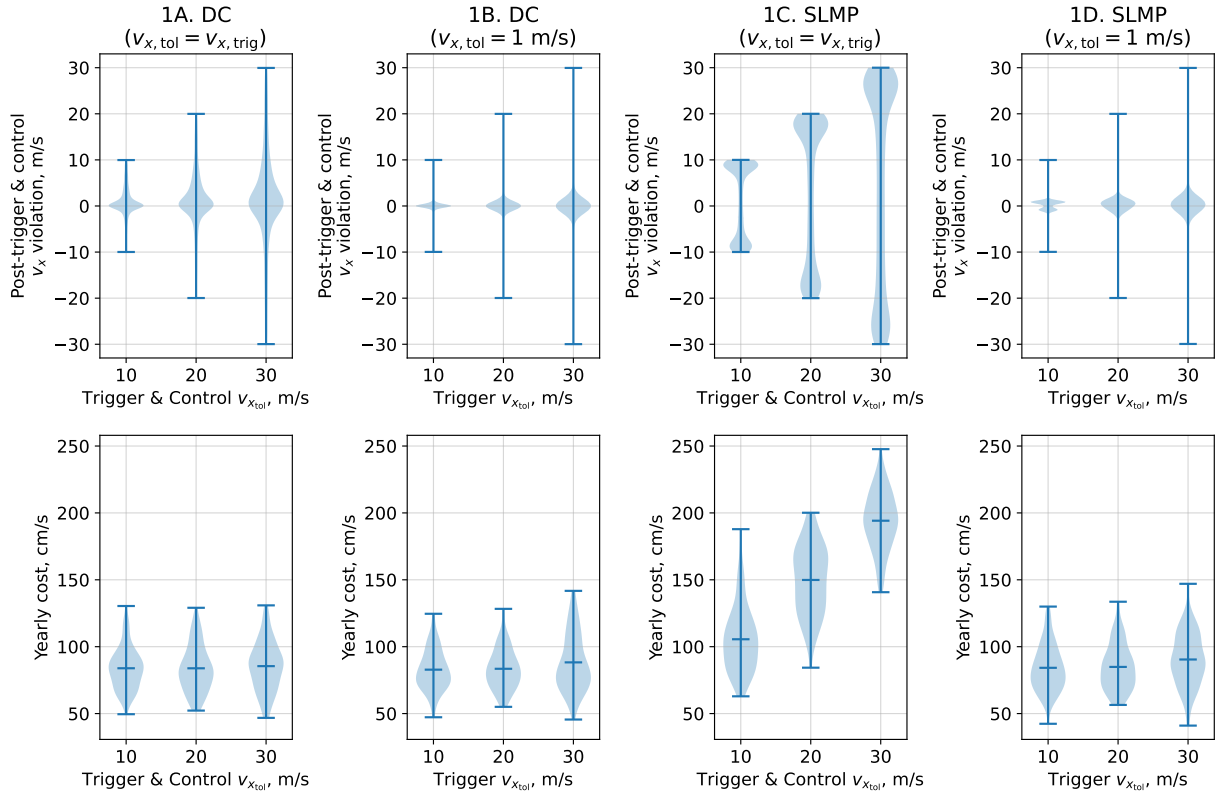


Fig. 11 Post trigger/control target violation and cumulative yearly cost with control schemes targeting v_x

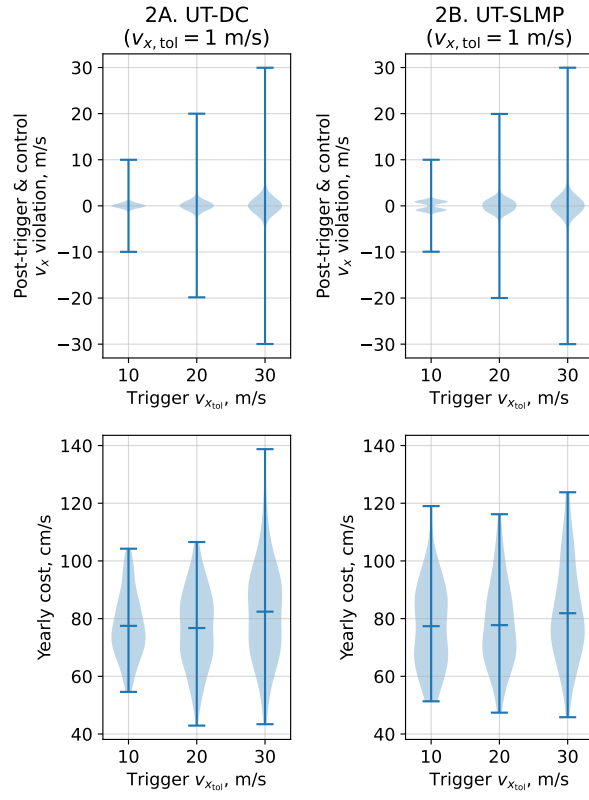


Fig. 12 Post trigger/control target violation and cumulative yearly cost with control schemes targeting $\mathbb{E}[v_x]$

Table 8 Summary of 100 Monte-Carlo runs comparing DC against UT-DC, using EKF with 3 measurements per revolution, $f = 360$ mm camera, $v_{x,\text{trig}} = 20$ m/s and $v_{x,\text{tol}} = 1$ m/s, maneuvering at a true anomaly of 180° .

Case	Controller	Success rate	Mean yearly ΔV , cm/s	95 th percentile yearly ΔV , cm/s	Max yearly ΔV , cm/s
1B	DC	100%	52.1766	77.4933	103.5663
2A	UT-DC	100%	47.9092	62.5284	76.1859

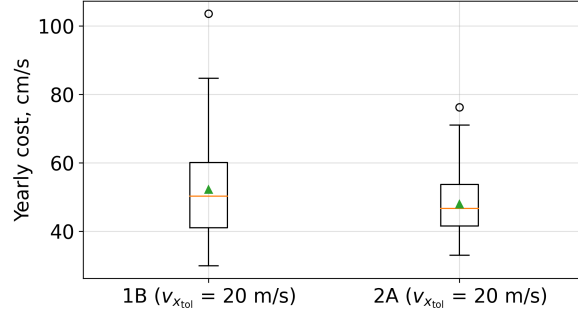


Fig. 13 Distribution of yearly station-keeping ΔV cost with full autonomous GNC pipeline, from 100 Monte-Carlo samples each; green triangle is the mean, and orange line is the median

configurations 1B and 2A, which were the cases with the best performance from the experiments in Section VI, without and with the UT-based targeting, respectively. In both cases, we select $v_{x,\text{trig}} = 20$ m/s and $v_{x,\text{tol}} = 1$ m/s.

A. Comparison against Filter-Only and Controller-Only Experiments

Table 8 summarizes the yearly ΔV , Figure 13 shows the distribution of the cumulative cost, and the corresponding cumulative cost histories are shown in Figure 14. The resulting ΔV are lower than those reported from the controller experiments in Tables 6 and 7, since the previously assumed $3\text{-}\sigma_r = 5$ km and $3\text{-}\sigma_v = 3$ cm/s were conservative. Figure 15 shows that the state estimate errors immediately before the maneuver are at lower values. Figure 16 shows the diagonal components of the covariance immediately before the maneuver, which are consistent with the empirical errors in Figure 15.

The relative performance between 1A and 2B is consistent both from Section VI and the GNC pipeline results presented here, where we see a substantial benefit from UT-based targeting. From Table 8, the advantage of UT is particularly pronounced in the 95th percentile and max cost from the Monte-Carlo experiments; as shown in Figure 14, out of the 100 Monte-Carlo samples, controller 2A has a smaller standard deviation, and there are few samples where the error realizations result in higher cumulative cost with controller 1B. While the same realizations are also apparent for controller 2A, the cumulative cost does not accumulate as fast as in 1B.

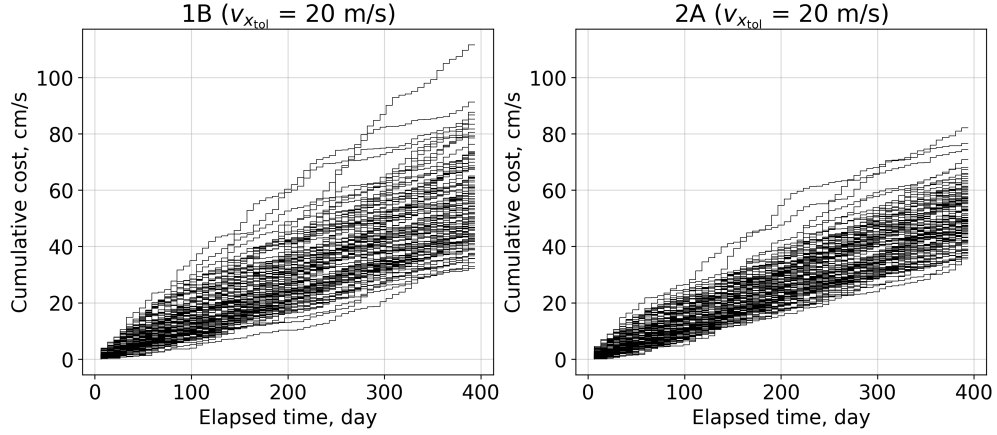


Fig. 14 Cumulative station-keeping cost with full autonomous GNC pipeline, from 100 Monte-Carlo samples each

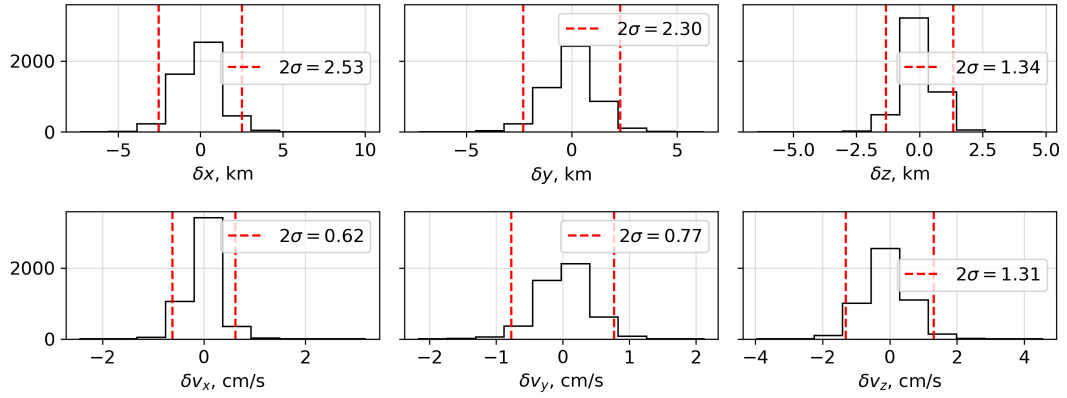


Fig. 15 Distribution of filter's state estimate error immediately before maneuver at a true anomaly of 180° . Red dashed lines correspond to the empirical 2σ bounds.

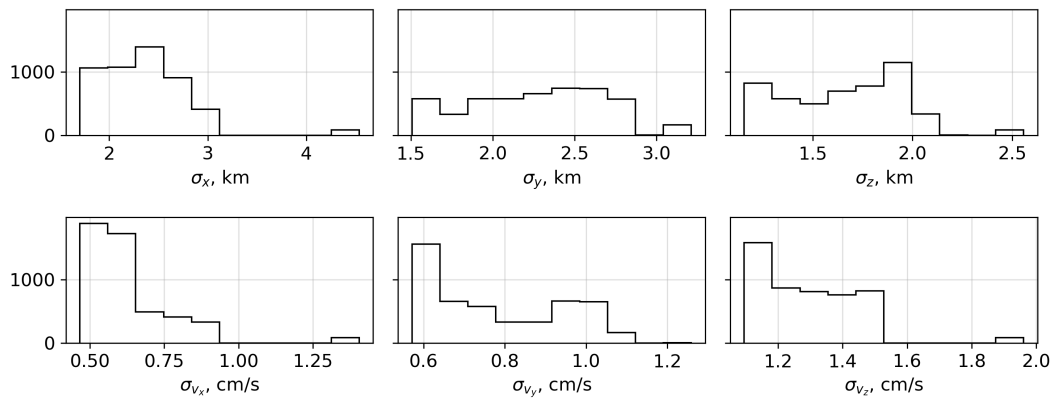


Fig. 16 Distribution of navigation filter's standard deviation immediately before maneuver at a true anomaly of 180°

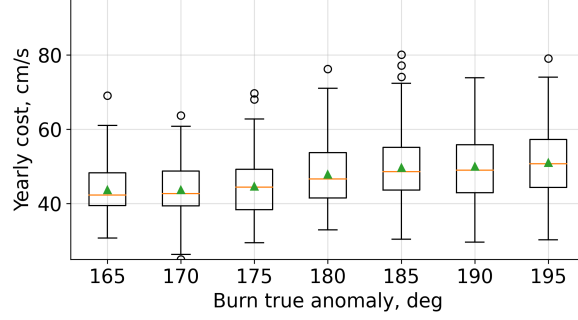


Fig. 17 Distribution of navigation filter’s standard deviation immediately before maneuver; green triangle is the mean, and orange line is the median

B. Sensitivity on Control Location

Guzzetti et al. [17] show that a constant covariance, for instance based on DSN measurements, results in a flat trend of total cumulative station-keeping cost against maneuver location. Using the full GNC pipeline consisting of the synthetic images and simulation of the navigation filters, we provide insight into the effect of the maneuver location with higher realism than assuming a fixed level of navigation error, as is common in control-only MC experiments that assume fixed navigation errors [16, 17, 19]. For this experiment, we adopt the UT-DC controller 2B, which was found to provide the best cost performance from results in VII.A.

Figure 17 shows the results from 100 Monte-Carlo runs, where the control action true anomaly is varied within a $\pm 15^\circ$ window about the apolune. While the average and median cost differences are below 10 cm/s, a larger discrepancy in the worst-case performance, exceeding a difference of 10 cm/s, is observed. Specifically, with respect to the considered NRHO, camera properties, and measurement frequency, maneuvering at a true anomaly of 170° yields the best performance, both in terms of the mean/median, and worst-case cumulative costs. We can interpret the small, albeit non-negligible difference in these yearly cost distributions by looking at the filter standard deviations from Figure 8. The minimum in σ_{v_z} occurs at around 170° , which coincides with the best-performing maneuver location in Figure 17. Such an observation is made possible by the realistic assessment that couples the navigation filter performance with station-keeping, especially in cases where a constant navigation covariance is not applicable.

VIII. Conclusion

Several key insights have been obtained from the development and evaluation of the guidance, navigation, and control pipeline for operations in a Near Rectilinear Halo Orbit with horizon-based OPNAV.

From a navigation standpoint, the simulations demonstrate that only a limited number of horizon-based measurements are necessary for the filter to maintain sufficient state estimation accuracy on the NRHO. An investigation of the camera field of view and measurement locations along the orbit reveals notable variations in estimation error. Across all tested

Table 9 Summary of 100 Monte-Carlo runs on station-keeping cost with UT-DC controller, executing maneuver at varying true anomalies around apolune. All cases using EKF with 3 measurements per revolution, $f = 360$ mm camera, $v_{x,\text{trig}} = 20$ m/s and $v_{x,\text{tol}} = 1$ m/s.

Burn true anomaly, deg	Success rate	Mean yearly cost, cm/s	95 th percentile yearly cost, cm/s	Max yearly cost, cm/s
165	100%	43.7387	56.2019	69.0637
170	100%	43.7115	58.0249	63.6931
175	100%	44.6368	59.8371	69.7114
180	100%	47.9092	62.5284	76.1859
185	100%	49.7340	68.6846	80.0424
190	100%	50.0258	68.6872	73.8191
195	100%	51.0217	64.5657	79.0357

configurations, the filter covariance exhibits a persistent and well-defined periodic structure. The structure is attributed to the inherent degradation of horizon-based measurement precision with increasing true anomaly, driven primarily by the rapid reduction in the apparent diameter of the Moon.

On the control side, the quasi-Newton convergence properties of differential correction provide an advantage in reducing cumulative station-keeping cost compared to an explicit minimization-based strategy. The lower performance of the latter arises from its short-sighted per-maneuver cost objective that only satisfies the targeting constraint to a specified tolerance, which does not directly minimize the overall cumulative cost. The introduction of hysteresis improves the performance for both differential correction and minimization-based approaches, as choosing a smaller targeting tolerance than the triggering tolerance enhances robustness against maneuver execution error and model uncertainty. Additionally, incorporating an unscented transform-based targeting framework substantially reduces the 95th-percentile and worst-case station-keeping costs observed in Monte Carlo simulations. By leveraging the filter covariance rather than relying solely on the state estimate, the unscented transform-based framework mitigates sensitivity to estimation errors, which vary considerably across realizations. Finally, the adoption of OPNAV-based navigation introduces a periodic structure in the filter covariance, which directly influences station-keeping performance, as the cumulative station-keeping cost becomes dependent on the maneuver location along the NRHO.

The OPNAV-based GNC pipeline developed in this work can be extended to a broader class of libration point orbits for which horizon-based OPNAV is applicable. Beyond horizon-based techniques, alternative OPNAV methods such as crater-based navigation and visual odometry may be considered to further enhance autonomous onboard navigation and reduce reliance on ground-based updates.

Acknowledgments

The authors acknowledge Pedro Miraldo for his help with setting up the synthetic image generation, as well as Marcus Greiff and Purnanand Elango for their advice on the implementation of the navigation filter and the minimization-based control schemes, respectively.

References

- [1] Lee, D. E., “Gateway Destination Orbit Model: A Continuous 15 Year NRHO Reference Trajectory,” , 2019.
- [2] Zimovan-Spreen, E. M., Howell, K. C., and Davis, D. C., “Near rectilinear halo orbits and nearby higher-period dynamical structures: orbital stability and resonance properties,” *Celestial Mechanics and Dynamical Astronomy*, Vol. 132, No. 5, 2020. <https://doi.org/10.1007/s10569-020-09968-2>.
- [3] Zimovan-Spreen, E. M., Howell, K. C., and Davis, D. C., “Dynamical Structures Nearby NRHOs with Applications to Transfer Design in Cislunar Space,” *Journal of the Astronautical Sciences*, Vol. 69, No. 3, 2022, pp. 718–744. <https://doi.org/10.1007/s40295-022-00320-4>.
- [4] Christian, J. A., and Robinson, S. B., “Noniterative Horizon-Based Optical Navigation by Cholesky Factorization,” *Journal of Guidance, Control, and Dynamics*, Vol. 39, 2016, pp. 2757–2765. <https://doi.org/10.2514/1.G000539>, URL <https://arc.aiaa.org/doi/10.2514/1.G000539>.
- [5] Christian, J. A., “Accurate Planetary Limb Localization for Image-Based Spacecraft Navigation,” *Journal of Spacecraft and Rockets*, Vol. 54, 2017, pp. 708–730. <https://doi.org/10.2514/1.A33692>, URL <https://arc.aiaa.org/doi/10.2514/1.A33692>.
- [6] Christian, J. A., “A Tutorial on Horizon-Based Optical Navigation and Attitude Determination With Space Imaging Systems,” *IEEE Access*, Vol. 9, 2021, pp. 19819–19853. <https://doi.org/10.1109/ACCESS.2021.3051914>.
- [7] Franzese, V., Di Lizia, P., and Topputo, F., “Autonomous optical navigation for the lunar meteoroid impacts observer,” *Journal of Guidance, Control, and Dynamics*, Vol. 42, No. 7, 2019, pp. 1579–1586. <https://doi.org/10.2514/1.G003999>.
- [8] Balossi, C., Piccolo, F., Panicucci, P., Pugliatti, M., Topputo, F., and Capolupo, F., “Moon Limb-Based Autonomous Optical Navigation Using Star Trackers,” *46th Rocky Mountain AAS GN&C Conference*, 2024, pp. 1–19.
- [9] Yun, S., Tuggle, K., Zanetti, R., and D’souza, C., “Sensor configuration trade study for navigation in near rectilinear halo orbits,” *Advances in the Astronautical Sciences*, Vol. 171, Univelt Inc., 2020, pp. 2799–2812. <https://doi.org/10.1007/s40295-020-00224-1>.
- [10] Qi, D. C., and Oguri, K., “Investigation on Autonomous Orbit Determination in Cislunar Space via GNSS and Horizon-based Measurements,” *AAS/AIAA Space Flight Mechanics Meeting*, 2023. URL <https://www.researchgate.net/publication/368663934>.
- [11] Inman, R., Holt, G., Christian, J., Smith, K., and D’Souza, C., “Artemis I Optical Navigation System Performance,” *AIAA SciTech Forum and Exposition*, 2024, , No. January, 2024. <https://doi.org/10.2514/6.2024-0514>.

- [12] Krause, M., Thrasher, A., Soni, P., Smego, L., Isaac, R., Nolan, J., Pledger, M., Lightsey, E. G., Ready, W. J., and Christian, J., *LONESTar: The Lunar Flashlight Optical Navigation Experiment*, Springer US, 2024. <https://doi.org/10.1007/s40295-024-00452-9>, URL <http://arxiv.org/abs/2401.12198>.
- [13] Givens, M., Caudill, M., Bolliger, M., Qi, D., and Parker, J., “Assessing Horizon-based Optical Navigation in a Near Rectilinear Halo Orbit,” *47th Rocky Mountain AAS GN&C Conference*, 2025.
- [14] Shirobokov, M., Trofimov, S., and Ovchinnikov, M., “Survey of station-keeping techniques for libration point orbits,” *Journal of Guidance, Control, and Dynamics*, Vol. 40, No. 5, 2017, pp. 1085–1105. <https://doi.org/10.2514/1.G001850>.
- [15] Oguri, K., “Chance-Constrained Control for Safe Spacecraft Autonomy: Convex Programming Approach,” *2024 American Control Conference (ACC)*, 2024, pp. 2318–2324. <https://doi.org/10.23919/ACC60939.2024.10645008>.
- [16] Davis, D., Bhatt, S., Howell, K., Jang, J.-W., Whitley, R., Clark, F., Guzzetti, D., Zimovan, E., and Barton, G., “Orbit Maintenance and Navigation of Human Spacecraft at Cislunar Near Rectilinear Halo Orbits,” *AAS/AIAA Space Flight Mechanics Meeting*, 2017.
- [17] Guzzetti, D., Zimovan, E. M., Howell, K. C., and Davis, D. C., “Stationkeeping Analysis for Spacecraft in Lunar Near Rectilinear Halo Orbits,” 2017.
- [18] Newman, C. P., Davis, D. C., Whitley, R. J., Guinn, J. R., and Ryne, M. S., “Stationkeeping, Orbit Determination, and Attitude Control for Spacecraft in Near Rectilinear Halo Orbits,” *AAS Astrodynamics Specialists Conference*, 2018. URL <https://ntrs.nasa.gov/search.jsp?R=20180006800>.
- [19] Davis, D. C., Scheuerle, S. T., Williams, D. A., Miguel, F. S., Zimovan-Spreen, E. M., and Howell, K. C., “Orbit Maintenance Burn Details for Spacecraft in a Near Rectilinear Halo Orbit,” *AAS/AIAA Astrodynamics Specialists Conference*, 2022.
- [20] Cheetham, B., Gardner, T., and Forsman, A., “Cislunar autonomous positioning system technology operations and navigation experiment (Capstone),” *Accelerating Space Commerce, Exploration, and New Discovery conference, ASCEND 2021*, American Institute of Aeronautics and Astronautics Inc, AIAA, 2021. <https://doi.org/10.2514/6.2021-4128>.
- [21] Shimane, Y., Miraldo, P., Berntorp, K., Greiff, M., Elango, P., and Weiss, A., “High-Fidelity Simulation of Horizon-Based Optical Navigation with Open-Source Software,” *International Astronautical Congress (IAC)*, 2023. URL <https://www.merl.com/publications/TR2023-128>.
- [22] Elango, P., Di Cairano, S., Berntorp, K., and Weiss, A., “Sequential linearization-based station keeping with optical navigation for NRHO,” *AAS/AIAA Astrodynamics Specialist Conference*, 2022.
- [23] Verner, J. H., “Numerically optimal Runge-Kutta pairs with interpolants,” *Numerical Algorithms*, Vol. 53, 2010, pp. 383–396. <https://doi.org/10.1007/s11075-009-9290-3>.
- [24] Gough, B., *GNU scientific library reference manual*, Network Theory Ltd., 2009.

- [25] Christian, J. A., “Optical Navigation Using Iterative Horizon Reprojection,” *Journal of Guidance, Control, and Dynamics*, Vol. 39, 2016, pp. 1092–1103. <https://doi.org/10.2514/1.G001569>, URL <https://arc.aiaa.org/doi/10.2514/1.G001569>.
- [26] Hartley, R., and Zisserman, A., *Multiple View Geometry in Computer Vision*, 2nd ed., Cambridge University Press, New York, NY, USA, 2003.
- [27] Christian, J. A., “Optical Navigation Using Iterative Horizon Reprojection,” *Journal of Guidance, Control, and Dynamics*, Vol. 39, 2016, pp. 1092–1103. <https://doi.org/10.2514/1.G001569>, URL <https://arc.aiaa.org/doi/10.2514/1.G001569>.
- [28] “Blender - a 3D modelling and rendering package,” , 2018. URL <http://www.blender.org>.
- [29] Carpenter, J. R., and D’souza, C. N., “Navigation Filter Best Practices,” Tech. rep., 2018. URL <http://www.sti.nasa.gov>.
- [30] Särkkä, S., and Svensson, L., *Bayesian filtering and smoothing*, Vol. 17, Cambridge university press, 2023.
- [31] Tapley, B. D., Schutz, B. E., and Born, G. H., *Statistical Orbit Determination*, Elsevier Academic Press, 2004.
- [32] Särkkä, S., “On unscented Kalman filtering for state estimation of continuous-time nonlinear systems,” *IEEE Transactions on Automatic Control*, Vol. 52, No. 9, 2007, pp. 1631–1641. <https://doi.org/10.1109/TAC.2007.904453>.
- [33] Elango, P., Di Cairano, S., Kalabic, U., and Weiss, A., “Local Eigenmotion Control for Near Rectilinear Halo Orbits,” *Proceedings of the American Control Conference*, Vol. 2022-June, 2022, pp. 1822–1827. <https://doi.org/10.23919/ACC53348.2022.9867672>.
- [34] Shimane, Y., Ho, K., and Weiss, A., “Optimization-Based Phase-Constrained Station-Keeping Control on Libration Point Orbit,” *AAS/AIAA Astrodynamics Specialist Conference*, 2024, pp. 1–19.
- [35] Shimane, Y., Di Cairano, S., Ho, K., and Weiss, A., “Revolution-Spaced Output-Feedback Model Predictive Control for Station Keeping on Near-Rectilinear Halo Orbits,” *IEEE Transactions on Control Systems Technology*, 2025. <https://doi.org/10.1109/TCST.2025.3614324>.
- [36] Muralidharan, V., and Howell, K. C., “Leveraging stretching directions for stationkeeping in Earth-Moon halo orbits,” *Advances in Space Research*, Vol. 69, No. 1, 2022, pp. 620–646. <https://doi.org/10.1016/j.asr.2021.10.028>, URL <https://doi.org/10.1016/j.asr.2021.10.028>.
- [37] Bauschke, H. H., and Combettes, P. L., *Convex Analysis and Monotone Operator Theory in Hilbert Spaces*, 1st ed., Springer Publishing Company, Incorporated, 2011.